High-Spin S = 3/2 Ground State Aminyl Triradicals:

Toward High-Spin Oligo-Aza Nanographenes

Hui Zhang,^{†, #} Maren Pink,[‡] Ying Wang, ^{†,⊥} Suchada Rajca,[†] Andrzej Rajca^{†,*}

[†]Department of Chemistry, University of Nebraska, Lincoln, NE 68588-0304, United States.

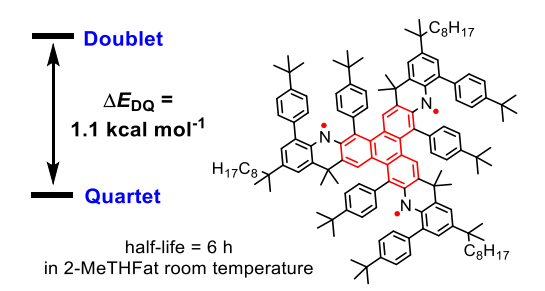
[‡]IUMSC, Department of Chemistry, Indiana University, Bloomington, IN 47405-7102, United States.

*Email: <u>arajca1@unl.edu</u>

Abstract:

We report high-spin aminyl triradicals with near-planar triphenylene backbones. Near planarity of the fused aminyl radicals and the 2,6,10-triphenylene ferromagnetic coupling unit (FCU), magnetically equivalent to three fused 3,4'-biphenyl FCUs, assures an effective $2p_{\pi}$ - $2p_{\pi}$ overlap within the crossconjugated π -system, leading to an S=3/2 (quartet) ground state that is well separated from low spin excited doublet states. Thermal populations of the low-spin ($S = \frac{1}{2}$) excited states are detectable both by SQUID magnetometry and EPR spectroscopy, providing doublet-quartet energy gaps, ΔE_{DO} , corresponding to 85+% population of the quartet ground states at room temperature. Notably, EPR-based determination of $\Delta E_{\rm DO}$ relies on direct detection of the quartet ground state and doublet excited state. The $\Delta E_{\rm DO}$ values are 1.0 – 1.1 kcal mol⁻¹, with the more sterically shielded triradical having the larger value. Half-life of the more sterically shielded triradical in 2-methyltetrahydrofuran (2-MeTHF) is about 6 h at room temperature. The less sterically shielded triradical in 2-MeTHF decomposes at 158 K with a halflife of about 4 h, while at 195 K, the half-life is still about 2 h. The dominant products of decay of triradicals are the corresponding triamines, suggesting the hydrogen atom abstraction from the solvent as the primary mechanism. This study expands the frontier of the open-shell PAHs/nanographenes, of which the unique electronic, nonlinear optical, and magnetic properties could be useful in the development of novel organic electronics, photonics, and spintronics.

TOC Graphics



INTRODUCTION

Organic radicals with high-spin ground states (total spin quantum number $S \ge 1$) and large energy gap (ΔE) between the high-spin ground state and low-spin excited state are promising building blocks for organic magnets, ¹⁻⁷ as well as multitude of emerging advanced materials based on spin chemistry. ⁸⁻¹⁷ Spin alignment in high-spin radicals is antithetical to the ubiquitous spin pairing in chemical bonds, ^{1,18,19} thus the design and synthesis of such radicals is of fundamental interest in chemistry and physics. To take advantage of the enhanced paramagnetic properties, which are scaled with factor S(S+1), the high-spin radicals should be persistent at room temperature and their high-spin ground states must be nearly exclusively populated. Consequently, the energy gap, ΔE , should be significantly greater than the thermal energy (RT) at 298 K, i.e., $\Delta E >> 0.6$ kcal mol⁻¹. Such diradicals and polyradicals are uncommon and, especially those with S > 1 are challenging to attain. ²⁰⁻³⁰

Polycyclic aromatic hydrocarbons (PAHs) have attracted great attention as building blocks for nanographenes. Our focus is on the PAH incorporating high-spin aminyl radicals with very strong ferromagnetic coupling between electron spins and with adequate stability at room temperature that would ultimately permit for isolation. The challenge is the design of PAHs as effective, strong ferromagnetic couplers.

We reported azaacene based aminyl diradicals 1 and 2, and tetraradical 3 that possess triplet and quintet ground states with large singlet triplet ($\Delta E_{\rm ST}$) and triplet quintet ($\Delta E_{\rm TQ}$) energy gaps of 1.7 – 5.5 kcal mol⁻¹, ³¹⁻³³ as predicted by the state-of-the-art dedicated difference configuration interaction (DDCI) calculations by Barone and coworkers (Figure 1). ^{34,35} In these structures, co-planarity of the aminyl radical and *m*-phenylene moieties facilitates the delocalization of spin density into the *m*-phenylene moiety, and thus large values of $\Delta E_{\rm ST}$ or $\Delta E_{\rm TQ}$. ^{1,31-33,36} The DDCI calculations on the nitroxide (R₂NO•) diradicals structurally related to 1 and 2 predict the $\Delta E_{\rm ST}$ values that are lower by one order of magnitude, ³⁴ comparable to $\Delta E_{\rm ST} \geq 0.6$ kcal mol⁻¹ measured by SQUID magnetometry for the related planar diazapentacene-based nitroxide diradical. ^{37,38} Analogously, we note one order of magnitude (factor of 20)

decrease in doublet-quartet energy gap, $\Delta E_{\rm DQ}$, from about 14 kcal mol⁻¹ estimated for planar 1,3,5-phenylene-based aminyl triradical³⁹ to $\Delta E_{\rm DQ} = 0.7$ kcal mol⁻¹ for resonance stabilized aminyl triradical 4.⁴⁰ The decreased energy gaps may be associated with diminished delocalization of spin density into the 1,3- or 1,3,5-phenylene ferromagnetic coupling unit, as observed in nitroxides and other organic radicals stabilized by resonance, ^{1,5,41} including triradical 4.⁴⁰ The resonance stabilization has been effectively utilized in the design of Blatter-based radicals with robust stability, such as the triplet ground state nitronyl nitroxide-Blatter, Blatter-Blatter diradicals ($\Delta E_{\rm ST} \approx 0.4$ –1.7 kcal mol⁻¹) and the quartet ground state triradical ($\Delta E_{\rm DQ} \approx 0.2$ –0.3 kcal mol⁻¹). Notably, the onset of thermal decomposition of these radicals was detected at temperatures between 160 and 264 °C.^{42,45} Likewise, analogous nitronyl nitroxide-oxoverdazyl radicals were reported but they possessed much lower $\Delta E_{\rm ST}$ = 0.29–0.39 kcal mol⁻¹ and $\Delta E_{\rm DQ}$ = 0.05 kcal mol⁻¹.^{46,47}

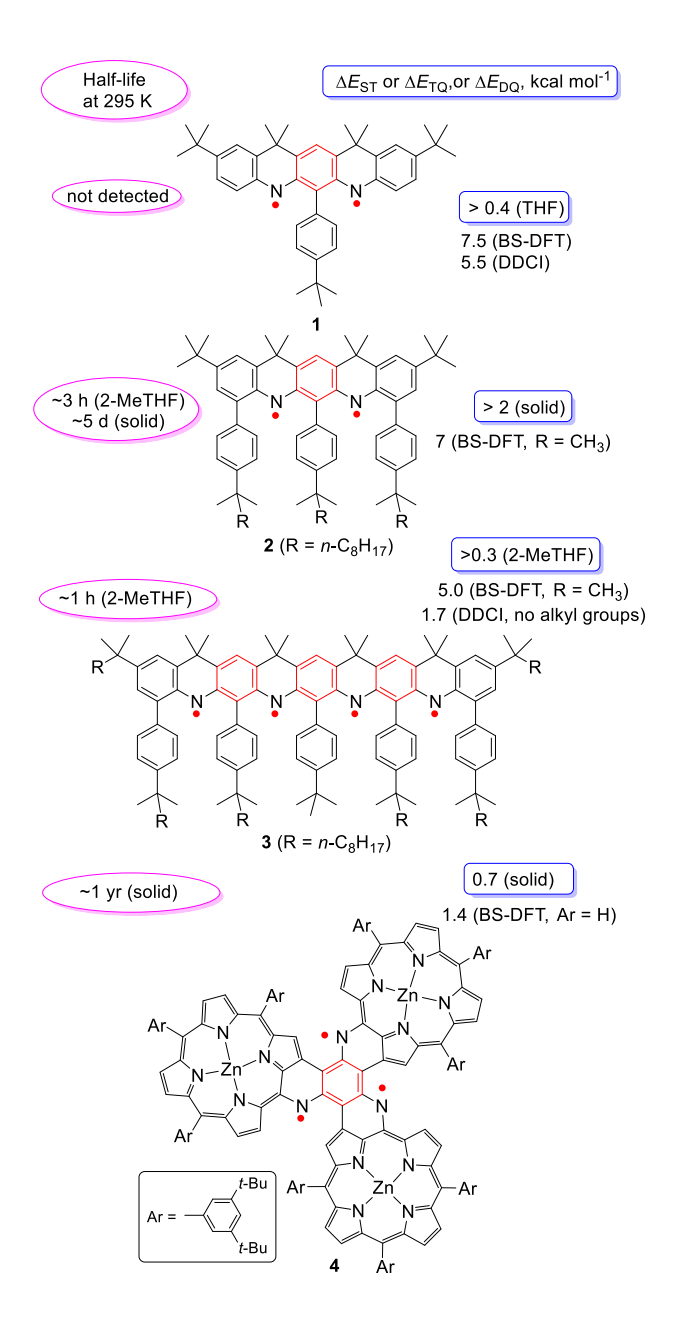


Figure 1. Persistent, high-spin ground state aminyl diradicals 1 and 2, tetraradical 3, and triradical 4. Half-life at room temperature; singlet-triplet, ΔE_{ST} (for 1 and 2), triplet-quintet, ΔE_{TQ} (for 3), and doublet-quartet, ΔE_{DQ} (for 4) energy gaps are determined experimentally by SQUID magnetometry and computationally by BS-DFT and DDCI.

Here we describe the synthesis and characterization of high-spin triphenylene based aminyl radicals, triradicals **5** and **6** (Figure 2), to explore and lay the groundwork for the design and synthesis of high-spin PAHs or nanographene. This study expands the frontier of the open-shell PAHs/nanographenes, predominantly based on the singlet (S = 0) ground state carbon-centered diradicals, which have been shown to possess unique electronic, nonlinear optical, and magnetic properties, that could be useful in the development of novel organic electronics, photonics, and spintronics.⁴⁸

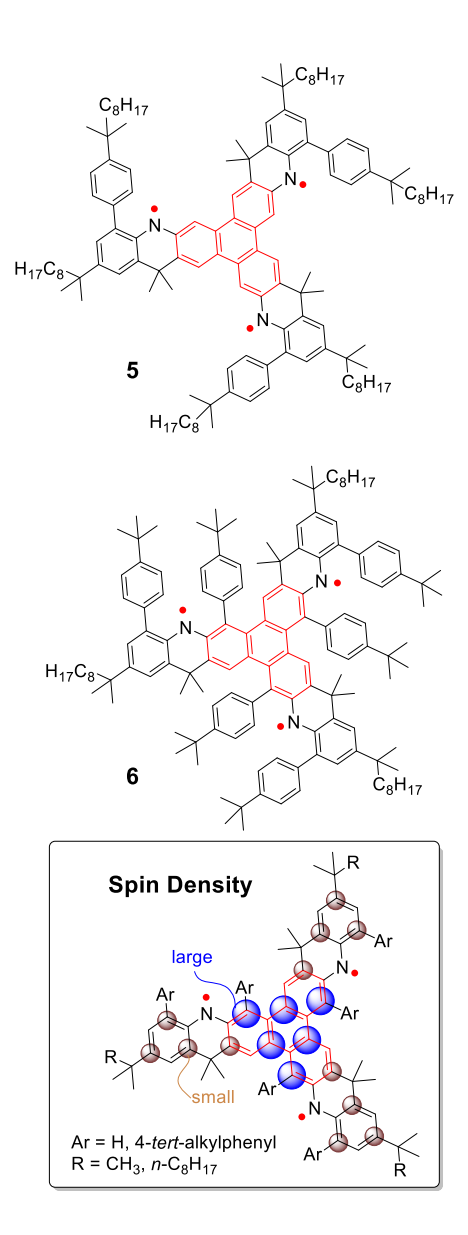


Figure 2. High-spin aminyl triradicals **5** and **6** with a 2,6,10-triphenylene ferromagnetic coupling unit. Spin densities are computed at the UB3LYP/6-31G(d) level of theory for an S = 3/2 state of C_{3h} -symmetric triradical **7** (Ar = H, R = CH₃); small and large spin densities correspond to ranges of 0.18-0.21 and 0.26-0.28 electrons, respectively (Tables S14 and S15, SI).

There are multiple reports of on-surface syntheses of various nanographene-like di- and polyradicals, however, these studies lack substantive evidence for their ground states and the underlying energy gaps. ⁴⁹⁻⁵⁷ Analogous reports on the syntheses and experimentally well-characterized high-spin ground states in solution/matrix or solid state are limited to the diradicals, such as the sterically protected triangulene and aza-triangulene cation. ^{58,59} We also note the recent report on "nitrogen-doped graphene" that displays ferromagnetic property at the C/N ratio less than 20.⁶⁰

Triradicals **5** and **6**, possessing 3 nitrogen atoms within 10 fused 6-membered rings, are simple and constitute a practical framework for exploring the feasibility of truly high-spin nanographene materials.⁴⁸ Near planarity of the fused aminyl radicals and the ferromagnetic coupling unit (FCU), 2,6,10-triphenylene, assures an effective $2p_{\pi}$ – $2p_{\pi}$ overlap within the cross-conjugated π -system, leading to an S = 3/2 (quartet) ground state that is well separated from low spin excited doublet states. A large doublet-quartet energy gap, ΔE_{DQ} , is predicted to be on the order of 3.5 kcal mol⁻¹ by the BS-DFT computation.

The 2,6,10-triphenylene FCU is magnetically equivalent to three fused 3,4'-biphenyl FCUs; that is, pairwise radical-radical interactions are within 3,4'-biphenyl units.⁶¹⁻⁶³ The carbon and nitrogen atoms with significant spin densities are sterically shielded to enhance persistence of triradicals but without significantly perturbing the co-planarity of aminyl radicals with 2,6,10-triphenylene (Figure 2).

The most sterically shielded triradical **6** with six 4-*tert*-butyphenyl pendants has a half-life of 6.4 h in 2-methyltetrahydrofuran (2-MeTHF) at room temperature. The analogous triradical **5** in 2-MeTHF, nonetheless, decomposes even at –115 °C (158 K) with a half-life of 3.9 h, and at 195 K, with a half-life smaller by a factor of only 2, which may imply the possible involvement of quantum mechanical tunneling.⁶⁴⁻⁶⁶

RESULTS AND DISCUSSION

Synthesis of Fused Triphenylene Triamines. Synthesis of the fused triamines **14** and **17** – **19** starts with oxidation of 2,6,10-tribromo-3,7,11-trimethyltriphenylene (**8**)^{67,68} to the corresponding tribromo tricarboxylic acid **9** (Scheme 1). Subsequent esterification of **9** gives triester **10**, which is then reacted with an excess of methylmagnesium bromide to provide triol **11**. Dehydration of **11** yields 2,6,10-tribromo-3,7,11-triisopropenyltriphenylene (**12**). Palladium-catalyzed C–N coupling reaction of **11** with 4-(1,1-dimethylnonyl)aniline produces triamine **13**, which is then subjected to Friedel-Crafts-like threefold annelation forming six-membered rings,^{69,70} to give fused triamine **14**.

To convert triamine **14** to hexa- and tri-bromo derivatives **15** and **16**, we apply our previously reported bromination method,³³ developed for ladder oligo(m-anilines) and rely on the similarity of oxidation potentials of bromine (Br₂, $E^{+/0} \approx 0.5$ V vs. SCE)⁷¹ and annelated diaryl amines ($E^{+/0} \approx 0.5$ V).⁶⁹ This

method, in which the electrophilic aminium radical cation (or triradical trication) intermediate is trapped with an excess of bromide under strictly anhydrous conditions at low temperature, gives 15 and 16 in good-to-excellent isolated yields.

Scheme 1. Synthesis of annelated triamines 17 - 19.

Using our standard conditions for the synthesis of hindered ladder oligo(*m*-anilines),^{32,72} the Suzuki coupling of the hexabromo triamine **15** with pinacol 4-*tert*-undecylphenylboronate³² does not provide detectable amounts of the target hexa-pendant substituted triamine, but rather the tri-pendant substituted triamine **17** is isolated in good yields. This suggests that the inner, more sterically hindered aryl-Br

moieties are reduced to the corresponding aryl-H moieties. Likewise, triamine 17 is the product of the Suzuki coupling of tribromo triamine 16 with pinacol 4-*tert*-undecylphenylboronate. The target triamine 18 is obtained in a good yield by Suzuki coupling with 4-*tert*-butylphenylboronic acid, using 2 M potassium carbonate in tetrahydrofuran (THF).⁷³ In addition to triamine 18, smaller amounts of pentapendant substituted triamine 19 are isolated.

Structure of Fused Triamines. The X-ray structure of triamine **18** shows that the triphenylene moiety is slightly distorted from planarity, with absolute values of torsional angles in the range of $6 - 25^{\circ}$ for the three bay areas, as illustrated by the torsional angles: C2-C1-C39-C38 = $-25.1(4)^{\circ}$, C25-C26-C27-C28 = $24.6(4)^{\circ}$, C12-C13-C14-C15 = $5.7(4)^{\circ}$ (Figure 3, top). Because the annelated aniline and triphenylene moieties are nearly co-planar, the annelated backbone of **18** appears to be approximately planar (Figure 3, middle). The amine (NH) moieties appear in a very congested environment, snuggled in-between the twisted 4-*tert*-butylphenyl pendant groups (Figure 3, bottom). The inner pendant groups are overcrowded as suggested by the outward bend of the C-C bond axes, which connect the pendant benzene rings to the annelated backbone, with angles in the $165 - 173^{\circ}$ range; torsion angles for the pendant benzene rings to the annelated backbone are in the $58 - 68^{\circ}$ range. The outer pendant groups are less overcrowded with their bend and torsion angles in the $172 - 176^{\circ}$ and $42 - 59^{\circ}$ ranges, respectively (Table S2, SI).

To gain better insight into the structures of these sterically hindered triamines with π -systems of angularly and collinearly fused six-membered rings, we carried out computational modeling. The simplified structures of **14**, **17**, and **18**, in which the *tert*-undecyl groups are replaced with *tert*-butyl groups (**14a**, **17a**, and **18a**), are studied at the B3LYP/6-31G(d,p) (or B3LYP/6-31G(d)) level of theory. Full geometry optimizations of these structures, **14a** and **17a**, with planar or twisted triphenylene conformations provide similar minimum energies – within about 1 kcal mol⁻¹. The lowest energy conformation for **18a**, which we were able to locate, belongs to the C_1 point group and it is obtained by starting the geometry optimization with the conformation corresponding to the X-ray structure of **18**.

The DFT-optimized geometry of the triphenylene in the lowest energy conformation of **18a** is similar to the X-ray structure of **18**, as indicated by the selected angles and torsional angles (Table S2, SI).

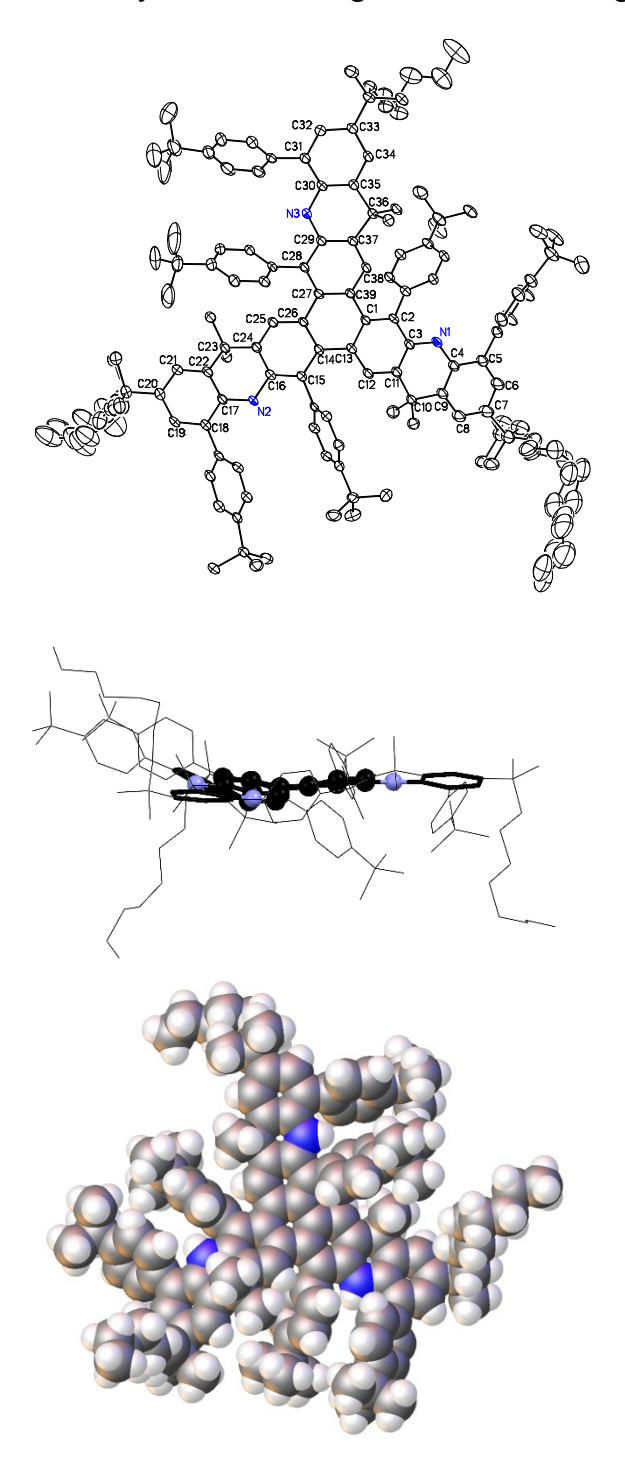


Figure 3. Molecular structure and conformation for triamine **18**, with disorder and a molecule of co-crystallized acetone omitted for clarity. <u>Top:</u> Ortep plot – top view of **18** with hydrogen atoms omitted; carbon and nitrogen atoms are depicted with thermal ellipsoids at 50% probability. <u>Middle:</u> Mercury-generated⁷⁴ side view of **18** with hydrogen atoms omitted, showing near co-planarity of annelated backbone, i.e., arylamine and 2,6,10-triphenylene moieties. <u>Bottom:</u> Space-filling plot of **18**. Further details are reported in Tables S1 and S2, and Figures S1–S3 in the SI.

Structures of the annelated triamine **14** and pendant-substituted triamines **17** and **18** are confirmed by the assignment of their experimental ¹H and ¹³C NMR spectra, using standard 2D NMR spectroscopy, including ¹H–¹³C HSQC, ¹H–¹³C HMBC, ¹H–¹H NOESY, and ¹H–¹⁵N HSQC (Figs. S53–S70, SI).

The correlation between the DFT-calculated (δ_{DFT}) and experimental (δ_{expt}) 1 H and 13 C NMR chemical shifts provides additional structural evidence for triamines **14**, **17**, and **18**. In particular, the linear regressions of δ_{DFT} vs. δ_{expt} (Figs. S49–S52, SI) give correlation coefficients, $R^2 = 0.9883 - 0.9955$ and 0.9968 - 0.9988, for 1 H and 13 C NMR chemical shifts, respectively; for **14a** and **17a**, the values of R^2 are higher for conformations with twisted vs. planar triphenylene moieties (Table S24, SI). The correlation between computed chemical shifts and δ_{expt} is further illustrated by the difference plots of the scaled and experimental NMR chemical shifts ($\delta_{scaled} - \delta_{expt}$) for all carbon or hydrogen atoms in the triamines (Figs. S49–S52, SI). These plots confirm our structure assignments by the low values of statistical error parameters for 13 C and 1 H (with the NH groups excluded) NMR chemical shifts (Table S24, SI). $^{77-79}$

Aminyl triradicals: oxidation of triamines. Triamine 17 or 18 (Equation 1) is subjected to the analogous oxidation reaction conditions to that implemented for the generation of high-spin aminyl radicals at low temperatures. A slight excess of n-BuLi over the stoichiometric amount of 3 equivalents is added to the triamine, and then the resultant trianion is oxidized by iodine, which is added by vacuum transfer in small portions (Equation 1). $^{31-33,72,80}$ In each case, the reaction mixture shows the expected half-field ($|\Delta m_S| = 2$) transition, while the $|\Delta m_S| = 1$ EPR spectral pattern, consisting of a center peak and multiple side bands, is distinct for the mixture from oxidation of 17 vs 18 (Figures 4 and 5).

Equation 1.

EPR spectroscopy and computational modeling. We were astonished that the oxidation product from triamine 17 shows an EPR spectrum in the $|\Delta m_S| = 1$ region (Figure 4) that could not be fit to either

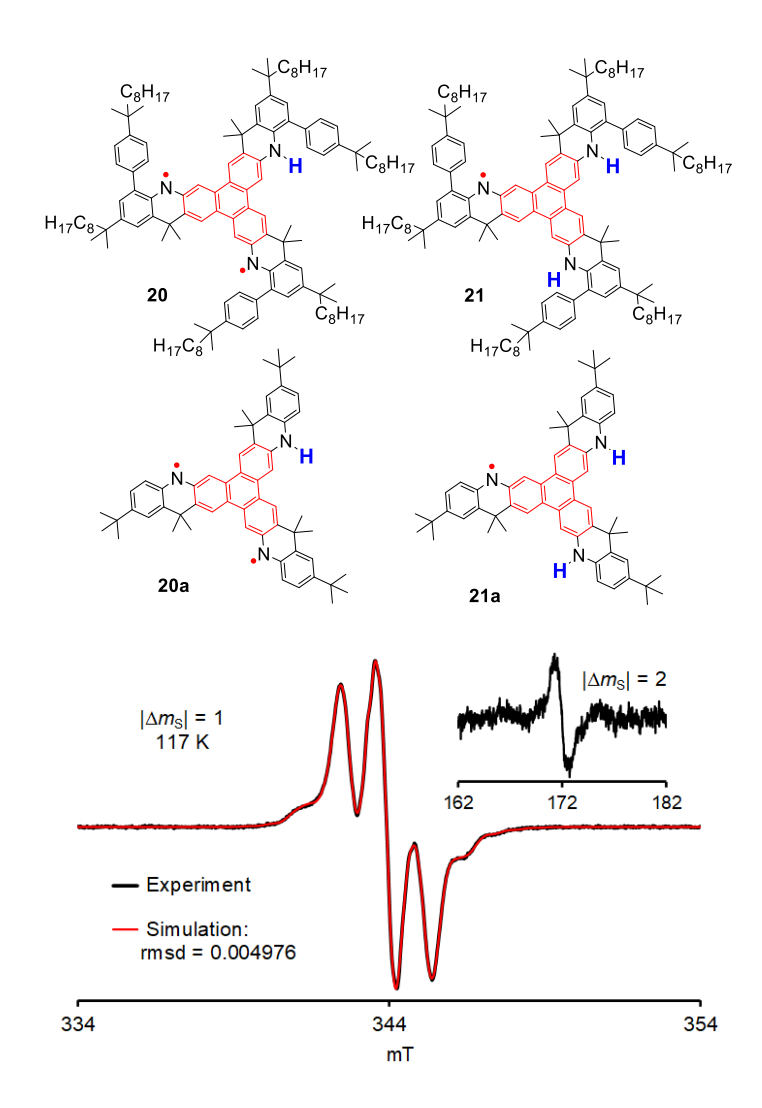


Figure 4. <u>Top:</u> Structures of diradical **20** and monoradical **21** – intermediate products of decay of S = 3/2 triradical **5** in 2-MeTHF, and their simplified computational models **20a** and **21a**. In the decay of **6**, analogous intermediate diradical **22** and monoradical **23** may be identified (Fig. S25, SI). <u>Bottom:</u> EPR (X-Band, v = 9.6441 GHz, $|\Delta m_S| = 1$; v = 9.6463 GHz, $|\Delta m_S| = 2$) spectrum of 0.93 mM **5** at 117 K (obtained by oxidation of **17**, eq. 1); $|\Delta m_S| = 2$ spectrum (inset plot) was obtained using 8.9 mM **5** (prior to dilution). Simulation of the $|\Delta m_S| = 1$ region (rmsd = 0.004976) using four components with S = 3/2, S = 1, $S = \frac{1}{2}$, and $S = \frac{1}{2}$ * excited state (relative content of 1.000 : 1.105 : 0.345 : 0.0282) provides an average $\chi T = 1.26$ emu K mol⁻¹ vs. $\chi T = 1.18$ emu K mol⁻¹, obtained according to spin counting. Additional information for this sample may be found in Table S5 and Fig. S12, SI.

S=3/2 or S=1 single species.⁸¹ To solve this puzzle, we first attempt to measure the product (χT) of magnetic susceptibility, χ , and temperature, T, by quantitative EPR spectroscopy, which requires multiple measurements at 117 K, alternating between the sample and the reference.^{45,72,82} In between those measurements, the sample is stored in a solid/liquid ethanol bath (T=-115 °C=158 K), which is at the identical temperature to that used in the final step of the typical sample preparation. We notice that our

 χT -values, which start at $\chi T \sim 1.2$ emu K mol⁻¹ – well below the theoretical value of $\chi T = 1.875$ emu K mol⁻¹ for a 100% population of S = 3/2 state – are decreasing significantly during the measurement of χT ; in fact, the fit to the first-order rate equation, $-\ln(\chi T)$ vs time, gives the half-life, $\tau_{1/2} = 10 \pm 1$ h at 156 K (Fig. S13, SI). Since the values of χT are measured at constant T = 117 K, they are related to values of χ and of double integrated EPR intensity (*DI*). Notably, the peak height (*PH*) for the outermost bands do slightly increase, while the *PH* for the inner and the center bands shows a significant decrease during the annealing of the sample for 5 or 7 h at 156 K. This suggests the presence of a mixture of paramagnetic species with considerably different half-lives.

After measuring the decay of the EPR signal for the crude reaction mixture at -78 °C and then at room temperature (Figure 4), we observe that the 1 H NMR spectroscopic and ESI MS analyses of resultant products show nearly pure starting triamine 17 (see: Tables S29 and S30, Figs. S72 and S73, SI), with the degree of purity of 17 obtained in the crude mixture varying from sample-to-sample (SI). These results suggest that the oxidation of 17 yields a mixture of paramagnetic and diamagnetic compounds. We postulate that product mixture consists of radical intermediates, such as S = 3/2 triradical 5, S = 1 diradical 20, S = 1/2 monoradical 21, and, perhaps, diamagnetic triamine 17, as well as $S = \frac{1}{2}$ * excited state of 5 (Figure 4). We then rely on computational modeling to aid the analysis of the products.

We use ORCA⁸³ to compute the D-, $A(^{14}N)$ -, and g-tensors for the model radicals, S = 3/2 triradicals 7 (Figure 2 and Table 3) and S (Table 3), S = 1 diradical S (Figure 4), and S = 1/2 monoradical S (Figure 4), to reveal the expected orientations of the S-tensors for the triradicals and the diradical. S (Figure 4), to reveal the expected orientations of the S-tensors for the triradicals and the diradical. S (and approximately parallel to the S-tensor oriented parallel to the S-tensor oriented parallel to the S-tensor, which must be oriented parallel to the S-tensor, or orbital axes (and approximately parallel to the largest components of S (Tables S21 and S22, SI). This implies that the largest components of S (Tables S21 and S (Tables S21 and S22, SI) orbital axes, S are S-triradicals and S (Tables S21 and S22, SI) orbital axes, S-triradicals and S-tensor, which must be oriented parallel to the S-tensor orbital axes, S-triradicals and S-triradicals a

experimental EPR spectral width for **5** is 4|D| < 250 MHz, while the computed **D**-tensor for the model, S = 3/2 triradical **5a** gives 4|D| of about 720 MHz. However, we anticipate that the computed values of A_{ZZ} and A_{YY} , scaled by a factor of 1/2S, i.e., $A_{ZZ}/2S = 18.84$, 19.53, and 59.40 MHz for **5a**, **7**, and monoradical **21a** (Figure 4), as well as $A_{YY}/2S \approx 29.5$ MHz (for **20a**) will be close to the experimental values. Based on computations, we discern the smallest components of g-tensor are g_{ZZ} for triradicals and monoradical **21** and g_{YY} for diradical **20**. 32,33

The spectral simulation of the $|\Delta m_S| = 1$ region of EPR spectra is carried out using four components: S = 3/2, S = 1, S = 1/2, and $S = \frac{1}{2}$ *, with the $S = \frac{1}{2}$ * component, corresponding to the excited state of triradical 5.81 The results obtained from thoroughly optimized simulations of 22 spectra for triradical 5 at 110–117 K (Tables S3, S5, and S6, SI) are summarized in Table 1. Rewardingly, the tensor orientations and the values of $A_{YY}/2S$ and $A_{ZZ}/2S$ for all four radical components are in accordance with either computations or the "back-of-envelope" predictions for $S = \frac{1}{2}$ "; that is, for $S = \frac{1}{2}$, A_{ZZ} is anticipated to be the largest component of the ^{14}N A-tensor with the observed values on the order of $A_{ZZ}/3$, because of the presence of three ¹⁴N over which spin density is delocalized. Thus, the effective seven-line spectral pattern $S = \frac{1}{2}$ * is quite distinct from the three-line spectrum with a much larger (factor of 3) A_{ZZ} coupling constant for S = 1/2 monoradical 21 (Fig. S19, SI). The average |D| = 70.7 MHz for diradical 20 (Table 1) is similar to |D| = 75 MHz ($|D/hc| = 0.0025 \text{ cm}^{-1}$) reported for the analogous triarylmethyl diradical. which is also based on 3,4'-biphenyl FCU.⁶¹ Most importantly, the relative fraction of S = 3/2 ground state vs $S = \frac{1}{2}$ * excited state provides an estimate of doublet-quartet energy gap, $3J/k = 479 \pm 10$ K (n =22 spectra) (Table 1), which is in excellent agreement with the $3J/k = 480 \pm 30$ K, obtained from SOUID magnetometry (Table 2). 44,86

Table 1. Summary of Analyses of EPR Spectra for Aminyl Diradical **2**, Tetraradical **3**, and Triradicals **5** and **6** in 2-MeTHF at 110 – 117 K.^a

	S	<i>D</i> (MHz)	E (MHz)	A _{YY} /2S (MHz)	Azz /2S (MHz)	gxx	g_{YY}	gzz	g	3J/k (K) [n]
Diradical 2	1	260	57.7	-	29.7	2.0030	2.0043	2.0019	2.0031	-
Tetraradical 3	2	154	48.0	15.0	1	2.0020	2.0016	2.0041	2.0026	ı
Triradical 5	3/2	36.5 ± 0.2	0.000	-	19.0 ± 0.1	2.0037	2.0037	2.0017	2.0030	479 ± 10 [22]
	1/2*	-	-	ı	20.2 ± 0.04	2.0045	2.0045	2.0021	2.0037	
	1	70.7 ± 0.4	2.8 ± 0.7	25.6 ± 0.2	ı	2.0033	2.0018	2.0045	2.0032	
	1/2	-	-	-	62.7 ± 0.3	2.0060	2.0034	2.0021	2.0038	
Triradical 6	3/2	35.9 ± 0.2	0.000	ı	17.3 ± 0.1	2.0038	2.0038	2.0025	2.0034	538 ± 5 [19]
	3/2	31.4 ± 0.3	7.2 ± 0.1	-	17.4 ± 0.1	2.0039	2.0038	2.0025	2.0034	
	1/2*	-	-	-	18.5 ± 0.1	2.0034	2.0037	2.0025	2.0032	
	1	60.8 ± 1.4	6.0 ± 0.8	25.2 ± 0.6	-	2.0031	2.0018	2.0038	2.0029	
	1/2	-	-	-	56.6 ± 0.2	2.0050	2.0031	2.0022	2.0034	

^a Data for diradical **2** and tetraradical **3** were obtained at 132 − 133 K.^{32,33} ^b For triradical **5**, values of 3*J/k* and parameters are given as average or average \pm SE based on 18 − 22 independent, 4-component fits (for 18 − 22 samples) with S = 3/2 (triradical), $S = \frac{1}{2}$ * (excited state, triradical), S = 1 (diradical **20**), and S = 1/2 (monoradical **21**) listed in Tables S3, S5, and S6, SI. ^c For triradical **6**, values of 3*J/k* and parameters are given as average or average \pm SE based on 11 − 21 independent, 4- or 5-component fits with S = 3/2 (triradical, C_3 -symmetry), S = 3/2 (triradical, C_1 -symmetry), $S = \frac{1}{2}$ * (excited state, triradical), S = 1 (hexa-pendant substituted diradical **22**, Fig. S25, SI), or S = 1/2 (hexa-pendant substituted monoradical **23**, Fig. S25, SI) listed in Tables S4, S7, and S8, SI. ^d $g \approx (g_X + g_Y + g_Z)/3$.

The product from triamine 18 oxidation shows a much more complex EPR spectrum in the $|\Delta m_S| = 1$ region (Figure 5), compared to that from triamine 17. We postulate that the mixture consists of C_1 - and C_3 -symmetric conformations of S = 3/2 triradical, of which the C_1 -symmetric S = 3/2 state is dominant. This is in qualitative agreement with DFT computations predicting that the lowest energy C_3 -symmetric quartet state of triradical 6a is about 1.8 kcal mol⁻¹ above the corresponding C_1 -symmetric conformation (Table 4, footnote b). Also, EPR spectra of the C_1 -symmetric S = 3/2 state are considerably more complex than that of the C_3 -symmetric counterpart.

We carry out the simulations of the EPR spectra with these two conformations as the initial structures and employ only one $S = \frac{1}{2}$ * excited state (C_1 -symmetric), to minimize the parameter dependence of the fits. We also add the 4th component, a hexa-pendant substituted S = 1 diradical 22 (Fig. S25, SI, this structure analogous to the tri-pendant substituted diradical 20 in Figure 4), which is a minor component (about 15%) in the freshly prepared samples of 6. Diradical 22 may originate from the incomplete reaction

of triamine **18** with *n*-BuLi (Equation 1). The simulated EPR spectra provide the \mathbf{D} -, $A(^{14}\text{N})$ -, and \mathbf{g} -tensor orientations (Table 1), as expected. Notably, both the values of D and $|A_{ZZ}|/2S$ for $\mathbf{6}$ are smaller than those for $\mathbf{5}$ (Table 1). This relationship agrees with the computed values of the ^{14}A -tensor for C_1 - and C_3 -symmetric $\mathbf{6a}$ (average $A_{ZZ}/2S = 17.9$ MHz) and $\mathbf{5a}$ ($A_{ZZ}/2S = 18.8$ MHz) (Tables S22 and S23, SI).

Based on the EPR spectra, the products appear to be persistent at T = -115 °C (158 K). The χT obtained by quantitative EPR spectroscopy, $\chi T = 1.72 \pm 0.02$ emu K mol⁻¹ at 117 K, agrees with that obtained from the EPR spectrum simulation, $\chi T = 1.72$ (Figure 5). These values of χT are somewhat below the value of $\chi T = 1.875$ emu K mol⁻¹ for 100% populated S = 3/2 state, because of the admixture of the S = 1 diradical 22 and the presence of the thermally populated $S = \frac{1}{2}$ * excited state of triradical 6. Notably, the relative fraction of C_3 - and C_1 -symmetric S = 3/2 ground states vs $S = \frac{1}{2}$ * excited state provides an estimate of the doublet-quartet energy gap, $3J/k = 538 \pm 5$ K (n = 19 spectra) (Table 1), which is in excellent agreement with the $3J/k = 540 \pm 30$ and 570 ± 40 K, obtained from SQUID magnetometry (Table 2). 44.86 These results unequivocally verify the high-spin (S = 3/2) ground state for triradical 6.

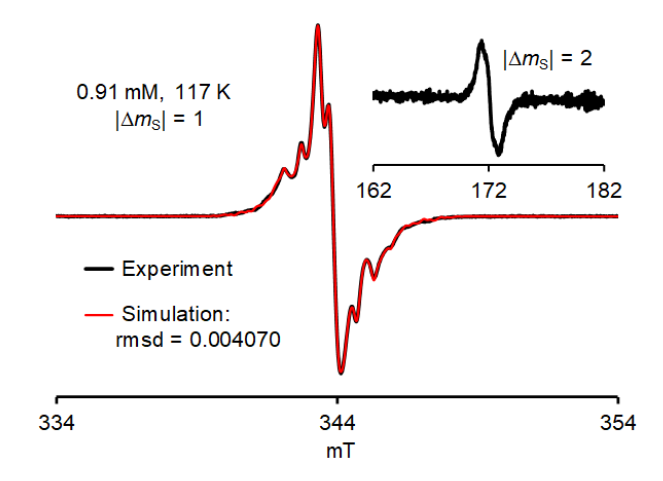


Figure 5. EPR (X-Band, v = 9.6421 GHz, $|\Delta m_S| = 1$; v = 9.6488 GHz, $|\Delta m_S| = 2$) spectrum of 0.91 mM 6 at 117 K; $|\Delta m_S| = 2$ spectrum (inset plot) was obtained using 9.7 mM 6 (prior to dilution). Simulation of the $|\Delta m_S| = 1$ region (rmsd = 0.004070) using four components with S = 3/2 (triradical, C_3 -symmetry), S = 3/2 (triradical, C_1 -symmetry), $S = \frac{1}{2}$ * (excited state, triradical), S = 1 (hexa-pendant substituted diradical 22, Fig. S25, SI) with relative content of 1.000 : 6.485 : 0.0637 : 1.483) provides an average $\chi T = 1.72$ emu K mol⁻¹ vs. $\chi T = 1.72 \pm 0.02$ (n = 6) emu K mol⁻¹, obtained by quantitative EPR spectroscopy (spin counting), using Tempone as reference. Additional information on this sample may be found in Table S7 and Fig. S26, SI.

Magnetic characterization of triradicals: EPR spectroscopy followed by SQUID magnetometry.

Custom made flame-sealable quartz tubes that allow for monitoring of the reaction mixture by EPR spectroscopy are used for preparation of the triradicals and the consecutive EPR/SQUID/EPR measurements.^{33,87} Notably, a one order-of-magnitude increased concentration of radicals is required for SQUID magnetometry, compared to that for EPR spectroscopy. Thus, the samples of concentrated bright green solutions of triradicals **5** and **6** in 2-MeTHF at 110 K, show broadened EPR spectra in the $|\Delta m_S|$ = 1 region (Figures 6 and 7), compared to those in Figures 4 and 5.

SQUID Magnetometry. Magnetic studies of **5** and **6** in 2-MeTHF by SQUID magnetometry unequivocally confirm their quartet ground states, as evidenced by the approximate S = 3/2 paramagnetic behavior in both the magnetization (M) vs. magnetic field (H), and the product (χT) of magnetic susceptibility (χ) and temperature (T) vs. T plots (Figures 6 and 7, and Table 2). We found that it is essential to allow for long equilibration times at each measurement temperature (up to 20 min) and to remove thoroughly traces of hexanes (solvent for n-BuLi), to preclude artificial hystereses at low temperatures (e.g., Fig. S11, SI).

The $M/M_{\rm sat}$ vs. $H/(T-\theta)$ plots for **5** and **6** at 1.8 – 5 K approximately follow that of the S=3/2 Brillouin function. The curvature of the plots, which does not depend on the radical concentration or the amount of sample, indicates a major contribution from the $S \approx 3/2$ ground state. A mean-field parameter, with a typical value, $\theta \approx -0.1$ K, accounts for weak intermolecular antiferromagnetic interactions between the radicals. The magnetization at saturation, $M_{\rm sat}$, measures the spin concentration of the sample, as discussed below.

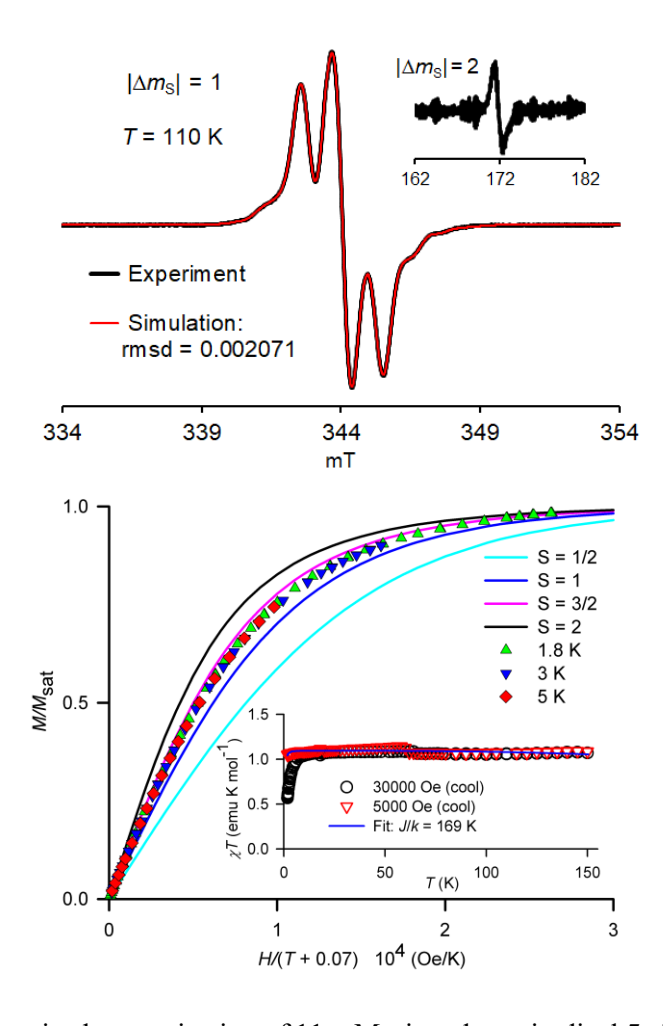


Figure 6. EPR/SQUID magnetic characterization of 11 mM tripendant triradical 5. Top: EPR (X-Band) spectrum in 2-MeTHF at 110 K prior to the SQUID magnetic studies. Inset plot: $|\Delta m_S| = 2$ region. Simulation of the $|\Delta m_S| = 1$ region (rmsd = 0.002071) using four components with S = 3/2, S = 1, S = 1/2, and $S = \frac{1}{2}$ * excited state (relative content of 1.000 : 0.523 : 1.254 : 0.00798) provides an average $\chi T = 1.03$ emu K mol⁻¹ vs. $\chi T = 1.08$ emu K mol⁻¹, obtained using SQUID magnetometry on the identical sample. Bottom: Main plot: the magnetization at 1.8, 3, and 5 K is plotted as $M/M_{\rm sat}$ vs. $H/(T - \theta)$ with Brillouin functions for S = 1/2, 1, 3/2, and 2. Inset plot: the magnetic susceptibility at 30000 Oe and 5000 Oe is plotted as χT vs. T together with the numerical fit (solid line) to Heisenberg Hamiltonian for S = 3/2 triradical (Eq. 2). Selected fitting parameters for the main and inset plots are summarized in Table 2. For additional information, see: Tables S3 and S12, and Figs. S4 and S5, SI.

The plots of χT vs T in the T=1.8-10 K range show a drop-off at lower temperatures, due to weak intermolecular interactions and paramagnetic saturation; at H=30000 Oe, the drop-off is much larger because of paramagnetic saturation effects associated with a larger magnetic field. The plots of χT vs T in the T=10-150 K range show a slight drop-off at higher temperatures, thus suggesting a thermal population of low-spin excited states. Numerical fits to Equation $2^{1,86}$ give a doublet-quartet energy gap,

3J/k, for **5** and **6**, as summarized in Table 2. These values are in good agreement with 3J/k, obtained by EPR spectroscopy (Table 1). Surprisingly, the doublet-quartet energy gap, $\Delta E_{DQ} = 1.0$ kcal mol⁻¹, for less sterically hindered **5** is slightly smaller than $\Delta E_{DQ} = 1.1$ kcal mol⁻¹ for **6**.

Equation 2.

$$\chi T = (1.118T/H)N_{32}[\text{Nom/Denom}] \tag{2}$$

where

Nom =
$$1.5\sinh(1.5a) + 0.5\sinh(0.5a) + 2*[\sinh(0.5a)]*\exp((-3J/k)/T)$$

Denom = $\cosh(1.5a) + \cosh(0.5a) + 2*[\cosh(0.5a)]*\exp((-3J/k)/T)$
 $a = 1.345(H/(T - \theta))$

The fitted values of weight factor, $N_{32} = 0.58$ –0.59, in the χT vs. T plots for triradical **5** are significantly lower than those for triradical **6**, $N_{32} = 0.72$ –0.73 (Table S12, SI). A similar trend is observed for the values of $M_{\rm sat}$ expressed in $\mu_{\rm B}$, corresponding to the fraction of unpaired electron per aminyl radical site, i.e., spin concentration. Values of $M_{\rm sat} = 0.63$ $\mu_{\rm B}$ for **5** and $M_{\rm sat} = 0.73$ –0.78 $\mu_{\rm B}$ for **6** suggest significantly higher spin concentrations for **6** vs **5** (Table 2). Both N_{32} and $M_{\rm sat}$ for **5** and **6** are obtained based on the amount of the corresponding triamines used for the sample preparation. These trends are in line with the fits to EPR spectra, showing a significantly greater content of S = 3/2 triradical for samples of **6**, compared to those of **5** (Figures 6 and 7, Tables S3 and S4, SI). When the measured value of $\chi T_{\rm max} = 1.08 - 1.35$ emu K mol⁻¹ is corrected by the spin concentration ($M_{\rm sat}$ expressed in $\mu_{\rm B}$), the value of $\chi T_{\rm max}/M_{\rm sat} = 1.70 - 1.74$ emu K mol⁻¹, which is below the theoretical value of 1.875 emu K mol⁻¹, is as expected for an S = 3/2 triradical with an admixture of lower spin species (and a non-negligible population of S = 1/2* excited state).

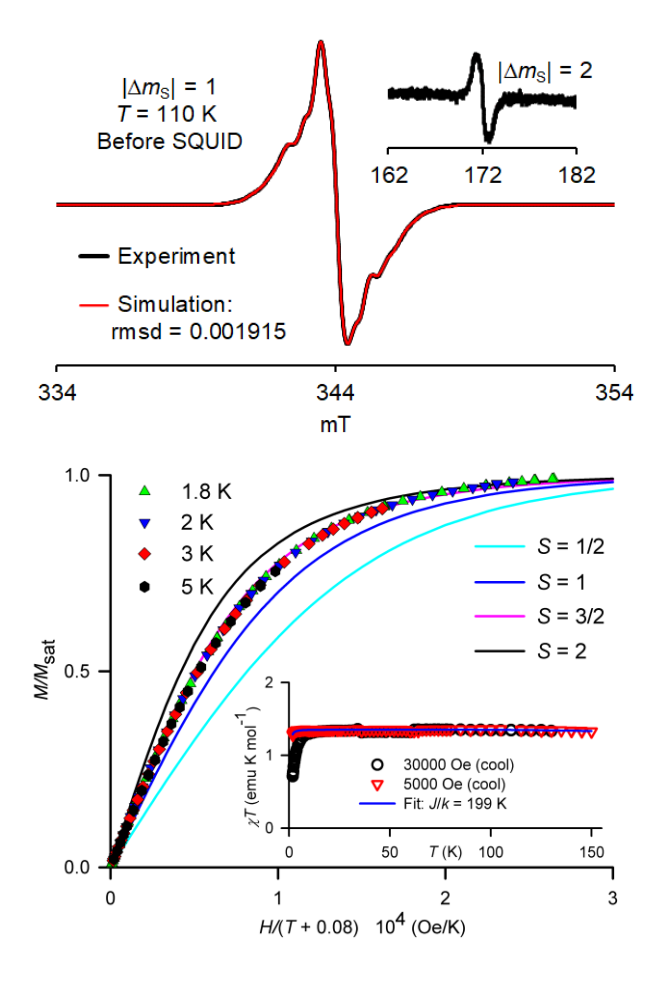


Figure 7. EPR/SQUID magnetic characterization of 17 mM 6 in 2-MeTHF. Top: EPR (X-Band) spectrum in 2-MeTHF at 110 K prior to the SQUID magnetic studies. Inset plot: $|\Delta m_S| = 2$ region. Simulation of the $|\Delta m_S| = 1$ region (rmsd = 0.001915) is carried out using four components S = 3/2 (C_3 -symmetric 6), S = 3/2 emu K mol⁻¹ vs. $\chi T/M_{sat} = 1.74$ emu K mol⁻¹ at 110 K, obtained using SQUID magnetometry on the identical sample. Bottom: Main plot: the magnetization at 1.8, 2, 3, and 5 K is plotted as M/M_{sat} vs. $H/(T - \theta)$ with Brillouin functions for S = 1/2, 1, 3/2, and 2. Inset plot: the magnetic susceptibility at 30000 Oe and 5000 Oe is plotted as χT vs. T together with the numerical fit (solid line) to Heisenberg Hamiltonian for S = 3/2 triradical (Equation 2). Selected fitting parameters for the main and inset plots are summarized in Table 2. Additional information, including the EPR spectra after SQUID magnetometry and complete set of EPR simulation parameters, may be found in the SI: Tables S4 and S12, and Figs. S6–S11.

Table 2. Summary of Magnetic Data and Numerical Fits for Triradicals 5 and 6 in 2-MeTHF.

Triradical	Sample number	Mass ^a (mg)	Conc. ^b (mM)	S	$-\theta(K)$	$M_{ m sat}^{ m c} \ (\mu_{ m B})$	$\chi T_{\text{max}}^{\text{d}}$ (emu K mol ⁻¹)	$\chi T_{ m max}/M_{ m sat}$	3 <i>J/k</i> (K)
5	1	1.92	11	1.3	0.1	0.63	1.08	1.71	480 ± 30
6	1 2 3	3.36 2.42 1.57	20 17 9	1.5 1.4 1.4	0.7° 0.1 0.1	0.73 0.77 0.78	1.24 1.35 1.35	1.70 1.74 1.72	e 540 ± 30 570 ± 40

^a Mass of triamine 17 or 18. ^b Concentration based on the mass of triamine and the volume of solvent. ^c M_{sat} per mol of "monoamine moieties", i.e., aminyl radical site. ^d χT_{max} per mol of triamine measured at 30000 or 5000 Oe. ^e For this sample, residual hexanes may not have been removed as thoroughly as for other samples leading to increased value of the mean-field parameter $-\theta$ and artefacts in the χT vs T plots.

In summary, SQUID magnetometry establishes unequivocally that triradicals **5** and **6** in 2-MeTHF possess quartet ground states with the nearest electronic excited state (doublet) about 1.0 and 1.1 kcal mol⁻¹ higher in energy ($\Delta E_{DQ} = 1.0$ and 1.1 kcal mol⁻¹), respectively. These values of ΔE_{DQ} are in excellent agreement with those obtained from EPR spectroscopy, based on relative fractions of S = 3/2 ground and S = 1/2 excited states, as obtained from spectral simulations.

Decay Kinetics of Aminyl Triradicals. The persistence of aminyl triradicals, tri-pendant **5**, hexapendant **6**, and penta-pendant substituted **24** (Chart 1), in 2-MeTHF is investigated by EPR spectroscopy. (Triradical **24** was prepared based on the procedure for **5** shown in equation 1, with the final (oxidation) step carried out at –130 °C, i.e., 143 K.)

Chart 1. Penta-pendant substituted triradical 24, derived from triamine 19.

As observed earlier, tri-pendant substituted triradical **5** is undergoing decay even at -115 °C (158 K). The center peak height (*PH*) decays the fastest, with a half-life, $\tau_{1/2} = 5.8 \pm 0.2$ h, based on $-\ln(PH)$ vs time linear regression (Fig. S13, SI). Because the S = 3/2 triradical is a major contributor to the intensity of the center peak, with the $S = \frac{1}{2}$ monoradical having minor contribution (Fig. S19, SI), this $\tau_{1/2}$ should

be viewed as the upper bound, i.e., the actual half-life of S = 3/2 **5** at 158 K is less than 5.8 h. Indeed, the linear regression of the $-\ln(x)$ vs time ($R^2_{\text{adj}} = 0.9948$), where x is the corrected molar fraction of triradical (S = 3/2 and $S = \frac{1}{2}$ * states, *vide infra*), obtained from numerical fits to EPR spectra (Table S5, SI), gives $\tau_{1/2} = 3.84 \pm 0.14$ h for **5** at 158 K (Figure 8, Table 3).

For **5**, the decay of χT at 195 K is faster by a factor of about two, compared to that at 158 K; that is, linear regression of $-\ln(\chi T)$ vs time give $\tau_{1/2} = 5.3 \pm 0.3$ h at 195 K and $\tau_{1/2} = 10 \pm 1$ h at 158 K (Figs. S13 and S17, SI). Based on the linear regressions $-\ln(PH)$ vs time at 195 K, the center peak decays the fastest with $\tau_{1/2} = 3.00 \pm 0.37$ h at the initial stages, t = 0 - 75 min, but then slowing down to $\tau_{1/2} = 11.00 \pm 0.87$ h at the later stage, t = 135 - 495 min (Fig. S17, SI). This phenomenon may imply a shift from the dominant triradical decay to the decay of the monoradical.

To elucidate more rigorously the decay kinetics of **5**, we examine three consecutive first order irreversible reactions, starting with triradical (A) and ending with triamine (D) (Table 3). Molar fractions x of triradical (S = 3/2 and $S = \frac{1}{2}$ * states), diradical (B, S = 1 state) and monoradical (C, $S = \frac{1}{2}$ state) are obtained from the fits of EPR spectra. However, in the later stages of the decay, there is a significant amount of diamagnetic triamine product, which is not detected by EPR spectroscopy. Therefore, quantitative EPR spectra are obtained at each time point, using Tempone in 2-MeTHF, as a spin counting reference, 72 to provide the actual values of molar fractions in the presence of triamine. The resultant $\chi T_{\rm EPR}$ values are then matched to the $\chi T_{\rm cor}$ (fit), based on the spectral fits plus a contribution from diamagnetic triamine (Table S9, SI). The resultant corrected molar fractions, A(t), B(t), and C(t) for the triradical, diradical, and monoradical, respectively, are then fit to the integrated kinetic equations S1 – S3, SI. 32,88 To minimize parameter dependence in each fit, we use only two variable parameters, the starting molar fraction and the rate constant (Figure 8, Table 3, Table S11, SI). As expected, $k_1 > k_2 > k_3$ is obtained.

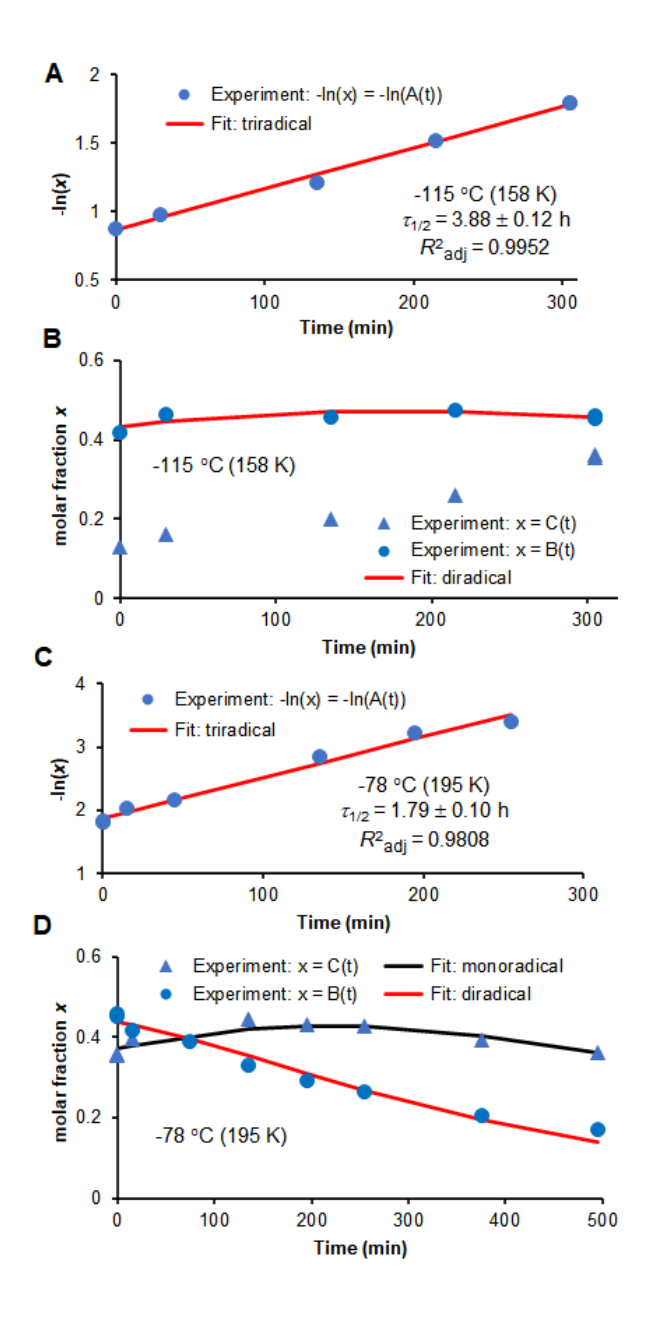


Figure 8. Decay kinetics of tri-pendant triradical **5** in 2-MeTHF at 158 and 195 K. At time = 0 min at 158 K, this sample was kept at approximately 158 K for about 8 h. **A:** decay at 158 K: linear regression $-\ln x$ vs t (eq. S1, SI) where x is the corrected molar fraction of triradical (A(t)). **B:** decay at 158 K: nonlinear regression, x vs t, where x is the corrected molar fraction of diradical **22** (B(t)), using eq. S2, SI. Analogous fits to the decay of monoradical **23** (C(t)), using eq. S3, SI, are unreliable (values of k_3 with P > 0.05). **C:** decay at 195 K: linear regression $-\ln x$ vs t (eq. S1, SI) where x is the corrected molar fraction of triradical (A(t)). **D:** decay at 195 K: nonlinear regressions, x vs t, where x is the corrected molar fraction of diradical **22** (B(t)) or monoradical **23** (C(t)), using eqs. S2 and S3, SI. More details may be found in Table 3 and the SI: Tables S9 and S11, Figs. S14 and S18.

Table 3. Kinetics of Decay of Aminyl Triradicals **5** and **6** in 2-MeTHF at 156 – 295 K.^a

		$A \xrightarrow{k_1} B \xrightarrow{k_2} C \xrightarrow{k_3} D$									
Triradical	<i>T</i> (K)	$k_1 (\text{min}^{-1}) \ [\tau_{1/2} (\text{h})]$	$R^2_{ m adj}$ [SEE]	$k_2 (\text{min}^{-1}) \ [\tau_{1/2} (\text{h})]$	$R^2_{ m adj}$ [SEE]	k ₃ (min ⁻¹) [τ _{1/2} (h)]	$R^2_{ m adj}$ [SEE]	$k_3 / k_2 / k_1$			
-	158	$2.98 \pm 0.09 \times 10^{-3}$ [3.88 ± 0.12]	0.9952 [0.0274]	$1.52 \pm 0.10 \times 10^{-3}$ $[7.61 \pm 0.48]$	0.52 [0.0130]	b	b	na:0.51: 1.00			
5	195	$6.44 \pm 0.37 \times 10^{-3}$ [1.79 ± 0.10]	0.9808 [0.0930]	$3.20 \pm 0.18 \times 10^{-3}$ [3.61 ± 0.20]	0.9664 [0.0200]	$2.25 \pm 0.09 \times 10^{-3}$ [5.14 ± 0.20]	0.8278 [0.0147]	0.35:0.50: 1.00			
6	295	$1.82 \pm 0.056 \times 10^{-3}$ $[6.35 \pm 0.20]$	0.9924 [0.0843]	$9.04 \pm 0.28 \times 10^{-4}$ [12.77± 0.40]	0.9908 [0.0191]	$6.33 \pm 0.27 \times 10^{-4}$ [18.26 ± 0.78]	0.9443 [0.0324]	0.35:0.50: 1.00			

^a Values of k_1 are obtained from linear regression and values of k_2 and k_3 from nonlinear regression, using eqs. S1 – S3, SI; SEE = standard error of estimate (eq. S5, SI). ^b Values of k_3 at 158 K are unreliable (P > 0.05), because the concentration of monoradical is still increasing in the investigated time frame, i.e., about 8 – 13 h at 158 K (Fig. S14, SI). More details may be found in Table S11, SI.

These rigorous analyses confirm that the decays of triradical (k_1) and diradical (k_2) at 195 K are faster than those at 158 K by a factor of 2 (Table 3). Such a relatively small increase in rate might suggest a contribution from hydrogen atom tunneling.⁶⁴⁻⁶⁶

For triradical **6**, the decay of the EPR intensity is nearly undetectable over 60 min at -30 °C (243 K); the initial decay at that temperature is non-first order, as indicated by $R^2 \approx 0.4$ for linear regression, $-\ln(DI)$ vs time, where $DI \sim \chi$ corresponds to double-integrated EPR intensity (Fig. S35, SI). However, the decay is readily detectable at 295 K. At the initial stage, e.g., t = 0 - 60 min, the relatively fast ($\tau_{1/2} \approx 2$ h), non-first order decay is most likely associated with the reaction of **6** with an excess of iodine (Figs. S23, S36, and S38, SI). After that period, the decay rate wanes, displaying first order kinetics, e.g., linear regression, $-\ln(DI)$ vs time, gives $\tau_{1/2} = 16.0 \pm 0.1$ h over the period of 40 - 6600 min with $R^2 = 0.9990$ (Fig. S23, SI).

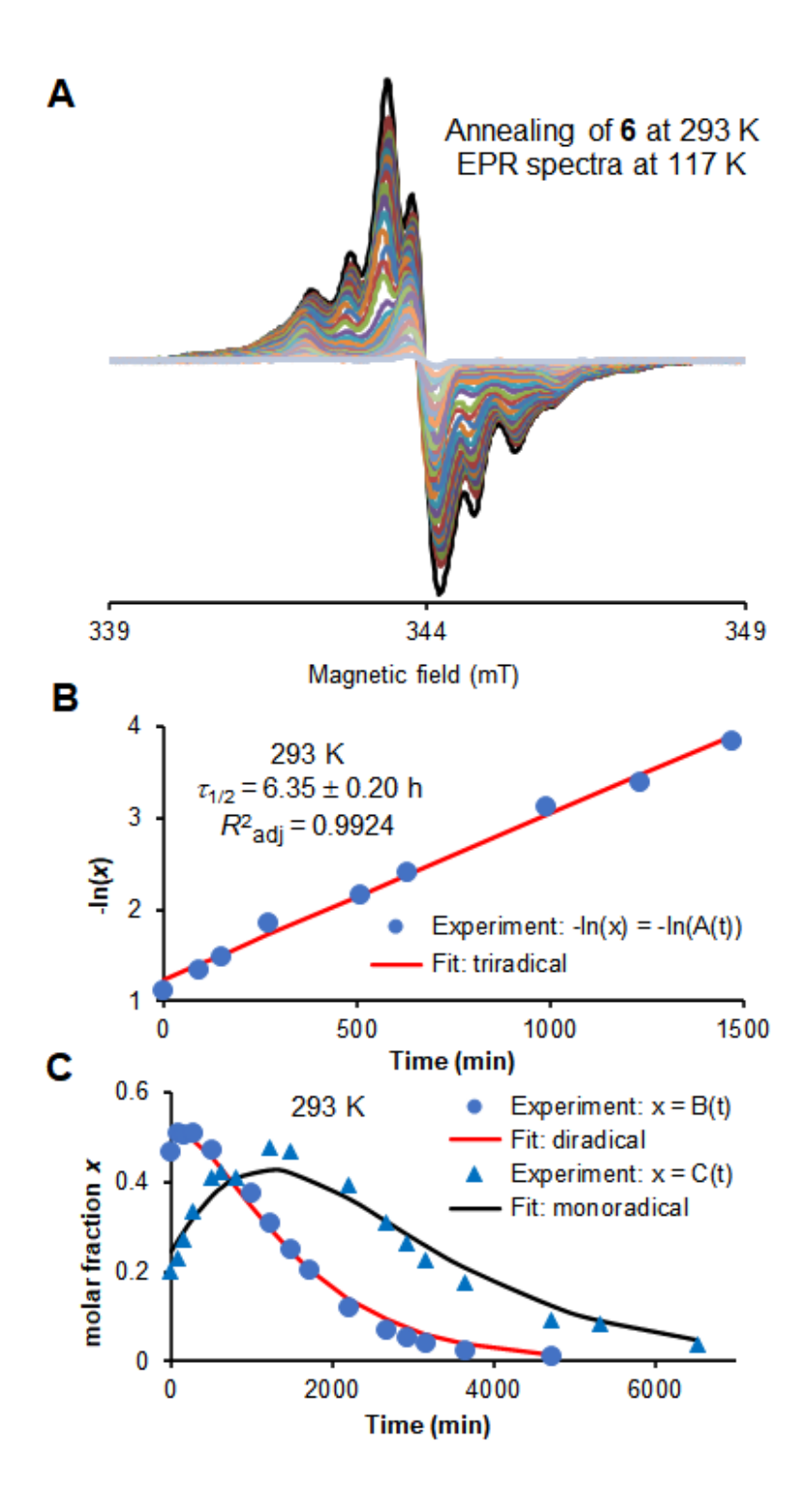


Figure 9. Decay kinetics of 0.91 mM triradical 6 in 2-MeTHF at 295 K. **A:** EPR spectra at 117 K after annealing at 293 K for 0 - 110 h. **B:** Linear regression $-\ln x$ vs t (eq. S1, SI) where x is the corrected molar fraction of triradical (A(t)). **C:** Nonlinear regressions, x vs t, where x is the corrected molar fraction of diradical **22** (B(t)) or monoradical **23** (C(t)), using eqs. S2 and S3, SI. More details may be found in Table 3 and the SI: Tables S10 and S11.

Following the procedure outlined for **5**, molar fractions x for **6** are obtained by simulations of EPR spectra, and then corrected for the presence of triamine. The values of corrected x are then fit to Eqs. S1 – S3 (SI), 32,88 to provide the rate constants, $k_1 > k_2 > k_3$ for **6** (Figure 9, Table 3 and Table S11). The half-life associated with k_3 for the decay of S = 1/2 monoradical **23** (Fig. S25, SI) is $\tau_{1/2} = 18.3 \pm 0.8$ h, which is within the range of half-lives $\tau_{1/2} = (18.4 - 20.2) \pm (0.03 - 0.6)$ h obtained from four linear regressions of the plots $-\ln(PH)$ vs t, with t being within the range of 1800–6600 min. The peak heights correspond to the center and the outermost bands that coincide with the spectrum of S = 1/2 monoradical **23** (Figs. S23, S24, S33, and S34, SI).

Also, we note that the ratios of rate constants, $k_3/k_2/k_1$, for the decays of **5** at 195 K (and $k_2/k_1 \approx 1:2$ at 158 K) and **6** at 295 K are identical, i.e., (2/3):1:2 (Table 3).

We analyze the decay kinetics of triradical 24 using double-integrated EPR intensities, $DI \sim \chi$, obtained from EPR spectra at 117 K. In contrast to 5, EPR spectra for 24 do not change over 2 h at 158 K, with – ln(DI) vs t showing no discernible correlation ($R^2 = 0.005 \approx 0.0$); also, at 195 K, the decay of DI is very slow ($\tau_{1/2} \sim 30$ h) and representing non-first order kinetics (Figs. S39 and S40). In contrast to 6, triradical 24 show appreciable first order decay at 243 K with $\tau_{1/2} = 12.8 \pm 1.1$ h ($R^2 = 0.9645$), based on linear regression $-\ln(DI)$ vs t in the period 0-6 h (Fig. S41, SI). The subsequent decay of **24** at room temperature (295 K) is according to first order kinetics ($R^2 > 0.99$) in the initial stage, 0 - 1 h, $\tau_{1/2} = 3.2 \pm 0.2$ h, and the subsequent two stages with increasing half-lives: 1.5 - 16 h, $\tau_{1/2} = 7.5 \pm 0.3$ h, and 21 - 75 h, $\tau_{1/2} =$ 19.7 ± 0.3 h (Fig. S42, SI). We assign these three consecutive stages to the decay of triradical, diradical, and monoradical, respectively. We find $k_1/k_2 \approx 2$, which is similar to the value obtained for 5 and 6, however, k_3 is relatively smaller. In other words, the triradical and diradical derived from 24 are decaying faster than those from 6, while the monoradicals derived from either 24 or 6 decay at similar rates. Similar to 5, for which the decay end product is the corresponding triamine, the decay products of 6 and 24 are predominantly triamines 18 and 19, according to ¹H NMR spectra and mass spectrometry of the isolated crude reaction mixtures (SI).

These results suggest that the decays of triradicals to triamines in 2-MeTHF proceeds by a hydrogen abstraction mechanism, 65,66,89 which is analogous to those observed for other high-spin aminyl radicals. 32,33,80 We observe that, under the same conditions, i.e. in 2-MeTHF at room temperature, the half-life of **6**, $\tau_{1/2} = 6.35 \pm 0.20$ h, is considerably longer than that of S = 1 diradical **2**, $\tau_{1/2} \approx 3$ h, or tetraradical **3**. $\tau_{1/2} \approx 1$ h. 32,33

DFT Computation of Doublet-Quartet Energy Gaps. The simplified structures of aminyl triradicals **5** and **6**, i.e., **5a**, **6a**, and **7** (Table 4), as well as diradical **20a** (Figure 4), are studied at the UB3LYP/6-31G(d)+ZPVE or UB3LYP/6-31G(d,p)+ZPVE levels of theory. Figure 4, are studied at the UB3LYP/6-31G(d)+ZPVE or UB3LYP/6-31G(d,p)+ZPVE levels of theory. Figure 4 and 7 in the high-spin (S = 3/2) states, starting from either planar or twisted conformations for the fused ring moieties, lead to energy minima corresponding to planar conformations with C_3 and C_{3h} point groups of symmetry, respectively. Geometry optimization of **6a**, starting with a conformation analogous to the X-ray structure of triamine **18**, predicts the lowest energy quartet state with a C_1 point group of symmetry. The C_1 -symmetric conformation is computed to be ca. 1.8 kcal mol⁻¹ below the lowest energy of a C_3 -symmetric conformation, which we can locate.

The triradicals in the low-spin ($S = \frac{1}{2}$) states are studied using broken-symmetry wave functions (BS-DFT). The doublet-quartet energy gap (ΔE_{DQ}) may be estimated using the energy gap between the ground state quartet and the lowest energy broken-symmetry doublet (ΔE_{UHF}), together with the correction for spin contamination (Equation 3). 90,91

Equation 3.

$$\Delta E_{\rm DQ} = \Delta E_{\rm UHF} \left[(\langle S^2_{\rm Q} \rangle - 0.75) / (\langle S^2_{\rm Q} \rangle - \langle S^2_{\rm BS-D} \rangle) \right]$$
 (3)

While this computational approach tends to overestimate the energy gaps for high spin ground states, 91,92 we obtain a rather small value of $\Delta E_{\rm DQ}$ for triradical **5a** compared to that for **7** with planar triphenylene moieties and for **6a** with twisted triphenylene moiety (Table 4). These results agree with the relative values of the experimental $\Delta E_{\rm DO}$, determined by EPR spectroscopy, for **5**, $3J/k = 479 \pm 10$

K, and for 6, $3J/k = 538 \pm 5$ K (Table 1). Although the spin density maps appear to be similar (Figure 10), the spin densities (Mulliken populations) within the triphenylene moieties of **5a** and C_1 -symmetric **6a** are distinguishable, i.e., the sums of positive spin densities at *ortho/para* positions in relation to the aminyl radicals is 2.18 and 2.35 electrons, respectively. Based on our empirical rule, 1,31 ΔE_{DQ} for **5a**, compared to that for C_1 -symmetric **6a**, is predicted to be smaller by the factor of $(2.18/2.35)^2 \approx 0.86$ vs the experimental factor of 0.89.

Table 4. Summary of Doublet-Quartet Energy Gaps (ΔE_{DQ}) for **5a**, **6a**, **7**, and **25a** and Singlet-Triplet Energy Gap (ΔE_{ST}) for **20a** by the BS-DFT at the UB3LYP+ZPVE Level.^a

Ar X 5a X = H, Ar = 4-tert-butylphenyl 6a X = Ar = 4-tert-butylphenyl 7 Ar = X = H										
		Basis set	State	$\langle S^2 \rangle$	ΔE_{UHF} (kcal mol ⁻¹)	$\Delta E_{\rm DQ}$ or $\Delta E_{\rm ST}$ (kcal mol ⁻¹)	J/k (K)			
5a	C_3	6-31G(d,p)	Quartet BS Doublet	3.886 1.840	2.00	3.07	515			
C-h	C_1	6-31G(d)	Quartet BS Doublet	3.894 1.837	2.25	3.45	579			
6a ^b	C_3	6-31G(d)	Quartet BS Doublet	3.905 1.844	2.46	3.76	631			
7	C_{3h}	6-31G(d)	Quartet BS Doublet	3.891 1.842	2.27	3.49	585			
20a	$C_{\rm s}$	6-31G(d)	Triplet BS singlet	2.086 1.058	1.12	2.28	574			
25a	C_3	6-31G(d)	Quartet BS Doublet	3.783 1.775	0.12	0.19	31			

^a Further computational details for **5a**, **6a**, and related radicals are provided in the SI (Tables S14 – S19). ^b The lowest energy C_3 -symmetric quartet state is 1.78 kcal mol⁻¹ above the C_1 -symmetric quartet ground state at the UB3LYP/6-31G(d)+ZPVE level of theory.

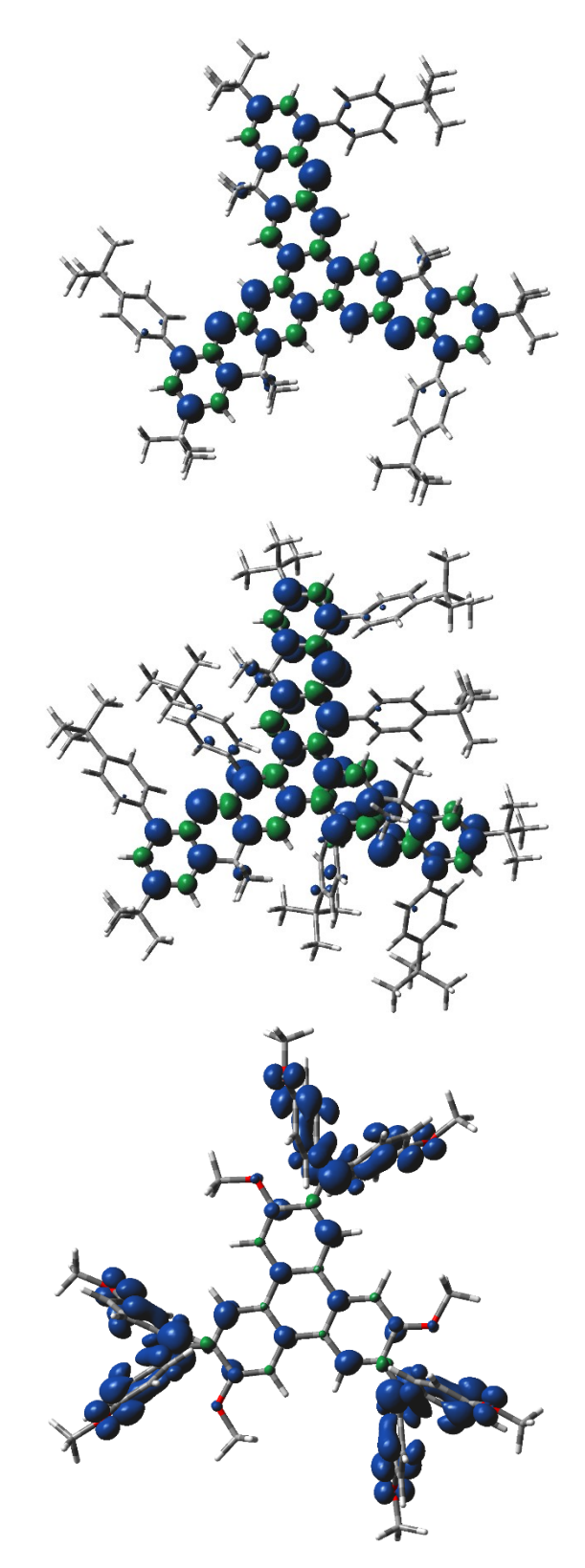


Figure 10. Spin density maps for the lowest energy quartet states with positive (blue) and negative (green) spin densities shown at the isodensity level of 0.003 electron/Bohr³. <u>Top:</u> triradical **5a** (UB3LYP/6-31G(d,p)). <u>Middle:</u> triradical **6a** (C_1 -symmetric, UB3LYP/6-31G(d,p)). <u>Bottom:</u> triradical trication **25a** (see: Chart 2).

As expected, according to the well-known tendency of BS-DFT to overestimate the stability of high-spin states, 91,92 the overall computed values of ΔE_{DQ} (and most likely, ΔE_{ST} for **20a**) significantly overestimate the experiment, i.e., by about a factor of three. Interestingly, the computed pairwise exchange coupling constant for triradicals **6a** and **7**, and diradical **20a** is J/k = 500 - 600 K, thus reflecting similar exchange coupling through each 3,4'-biphenyl ferromagnetic coupling unit within the triphenylene moiety. This is also confirmed by similar spin density maps for high spin ground states in triradicals **5a**, **6a**, and **7**, and diradical **20a** (Figure 10, Tables S14, S16, S18, and S19, SI).

Chart 2. Structure drawings of triradical trications 25 and 25a.

Fukuzaki and Nishide reported triphenylene-based triradical trication **25** (Chart 2) and concluded that this triradical possesses a nearly 100% population of the quartet state at room temperature and above. ⁹³ The conclusion was primarily based on the ¹H NMR Evans method ^{94,95} and there was no report on actual EPR spectra. We note that, in a molecule like **25**, very little spin density is expected within the triphenylene moiety, and thus the ΔE_{DQ} is expected to be miniscule, and perhaps even negative. This would imply a much lower constant value of magnetic moment (or χT), i.e., $\chi T = 0.375 * 3 = 1.125$ emu K mol⁻¹ for the three independent (uncoupled) unpaired electrons, compared to $\chi T = 1.875$ emu K mol⁻¹ for a 100% populated quartet state.

We carry out the DFT computations on **25a**, which is a minimally simplified version of **25** (Chart 2). Geometry optimization of the quartet state of **25a** started with fully co-planar aminium and triphenylene moieties and with a C_3 point group of symmetry constraint. The optimized minimum structure was quite twisted and possessed very little spin density within triphenylene moiety (Figure 10), with Mulliken populations suggesting a total of 0.60 electrons for the sum of positive spin densities at *ortho/para*

positions with respect to the aminium radical cations. Consequently, the DFT-computed $\Delta E_{DQ} = 0.19$ kcal mol⁻¹ for **25a** (Table 4) is lower by factor of 18, compared to ΔE_{DQ} for C_1 -symmetric **6a**, which is in a qualitative agreement with a factor of $(2.35/0.60)^2 \approx 15$, based upon spin densities within the triphenylene moieties. Because of the very small value of $\Delta E_{DQ} \approx 0.2$ kcal mol⁻¹, we may not preclude a possible lowspin (doublet) ground state for **25a** (and **25**), due to an overestimation of the stability the high-spin state by BS-DFT, 91,92 as illustrated in Tables 1, 2 and 4.

CONCLUSION

We have demonstrated that 2,6,10-triphenylene is an effective PAH ferromagnetic spin coupler. The near-planarity of the fused aminyl radicals and triphenylene backbone assures an effective $2p_{\pi}$ – $2p_{\pi}$ overlap within the cross-conjugated π -system. The S=3/2 (quartet) high-spin aminyl triradicals with triphenylene backbones are steppingstones to the high-spin oligo-aza nanographenes. The design, synthesis and characterization of the high-spin PAHs was challenging, especially the complex magnetic characterization.

We successfully developed two EPR-based protocols: (1) for determination of ΔE_{DQ} and (2) for measurement of half-lives of radicals in complex mixtures.

The determination of ΔE_{DQ} protocol relies on a direct detection of the quartet ground states and doublet excited states by spectral simulation of about 20 independent EPR spectra of radical mixtures. The simulations provide the relative contents of the ground and excited states, and thus allow for direct estimates of ΔE_{DQ} , which are in excellent agreement with the SQUID values.

The protocol for measurement of half-lives of radicals involves recording spectra of the radical mixture and of the spin counting reference at each time point. The spectral simulations permit identification of S = 3/2 triradical and the intermediate S = 1 diradicals and $S = \frac{1}{2}$ monoradicals, and thus provide an estimate of $\chi T(\text{fit})$ based on the relative content of radicals. To account for the diamagnetic products of the radical decay, a molar fraction of diamagnetic product in the radical mixture is adjusted until $\chi T_{\text{cor}}(\text{fit}) = \chi T_{\text{EPR}}$

(obtained by spin counting), thus providing corrected molar fractions of triradical, diradical and monoradical that are used to obtain the rate constants.

It is interesting to observe that the relative first-order rate constants for the decay of monoradicals, diradicals, and triradicals are 0.35:0.50:1.00, and this ratio does not depend on the degree of steric shielding in the three-fold symmetric triradicals. Half-life of the most sterically shielded triradical in 2-MeTHF is about 6 h at room temperature. The least sterically shielded triradical in 2-MeTHF decomposes at 158 K with a half-life of about 4 h, while at 195 K, its half-life is still about 2 h.

ASSOCIATED CONTENT

Supporting Information

General procedures and materials, additional experimental and computational details. This material is available free of charge via the Internet at http://pubs.acs.org.

Accession Codes

CCDC 2203738 contain the supplementary crystallographic data for this paper. These data can be obtained free of charge via www.ccdc.cam.ac.uk/data_request/cif, or by emailing data_request@ccdc.cam.ac.uk, or by contacting The Cambridge Crystallographic Data Centre, 12 Union Road, 495 Cambridge CB2 1EZ, UK; fax: +44 1223 336033.

AUTHOR INFORMATION

Notes

The authors declare no competing financial interests.

ACKNOWLEDGMENT

This research was supported by the National Science Foundation (CHE-1362454, CHE-1665256, and CHE-1955349) and National Institutes of Health, in particular EMX-plus upgrade of the Electron Paramagnetic Resonance (EPR) spectrometer (NIGMS R01GM124310-01). ChemMatCARS Sector 15 is principally supported by the National Science Foundation/Department of Energy under grant number NSF/CHE-1346572. Use of the Advanced Photon Source was supported by the U. S. Department of Energy, Office of Science, Office of Basic Energy Sciences, under Contract No. DE-AC02-06CH11357. We thank Dr. Przemysław J. Boratyński (now at Wrocław University of Technology) for the syntheses of 4-tert-undecylaniline and pinacol 4-tert-undecylphenylboronate.

PRESENT ADDRESSES

HZ: ZY Therapeutics, 400 Park Offices Dr #311, Research Triangle, NC 27709, USA

[⊥] YW: College of Chemistry, Beijing Normal University, Beijing 100875, China.

REFERENCES

- 1. Rajca, A. Organic diradicals and polyradicals: from spin coupling to magnetism? *Chem. Rev.* **1994**, 94, 871–893.
- 2. Rajca, A.; Wongsriratanakul, J.; Rajca, S. Magnetic ordering in an organic polymer. *Science* **2001**, 294, 1503–1505.
- 3. Ratera, I.; Veciana, J. Playing with organic radicals as building blocks for functional molecular materials. *Chem. Soc. Rev.* **2012**, *41*, 303–349.
- 4. Winkler, M.; Sander, W. Triradicals. Acc. Chem. Res. 2014, 47, 31–44.
- 5. Gallagher, N. M.; Olankitwanit, A.; Rajca, A. High-Spin Organic Molecules. *J. Org. Chem.* **2015**, *80*, 1291–1298.

- 6. Wingate, A. J.; Boudouris, B. W. Recent advances in the syntheses of radical-containing macromolecules. *J. Polym. Sci., Part A: Polym. Chem.* **2016**, *54*, 1875–1894.
- 7. Shimizu, D.; Osuka, A. Porphyrinoids as a platform of stable radicals. *Chem. Sci.* **2018**, *9*, 1408–1423.
- 8. Tan, Y.; Hsu, S.-N.; Tahir, H.; Dou, L.; Savoie, B. M.; Boudouris, B. W. Electronic and Spintronic Open-Shell Macromolecules, Quo Vadis? *J. Am. Chem. Soc.* **2022**, *144*, 2, 626–647.
- Gaudenzi, R.; de Bruijckere, J.; Reta, D.; Moreira, I. de P. R.; Rovira, C.; Veciana, J.; van der Zant,
 H. S. J.; Burzurí, E. Redox-Induced Gating of the Exchange Interactions in a Single Organic Diradical.
 ACS Nano 2017, 11, 5879–5883.
- Tsuji, Y.; Hoffmann, R.; Strange, M.; Solomon, G. C. Close relation between quantum interference in molecular conductance and diradical existence. *Proc. Natl. Acad. Sci. U.S.A* 2016, *113*, E413– E419,
- 11. Shil, S.; Bhattacharya, D.; Misra, A.; Klein, D. J. A high-spin organic diradical as a spin filter. *Phys. Chem. Chem. Phys.* **2015**, *17*, 23378–23383.
- 12. Sugawara, T.; Komatsu, H.; Suzuki, K. Interplay between Magnetism and Conductivity Derived from Spin-Polarized Donor Radicals. *Chem. Soc. Rev.* **2011**, *40*, 3105–3118.
- 13. Lee, J.; Lee, E.; Kim, S.; Bang, G. S.; Shultz, D. A.; Schmidt, R. D.; Forbes, M. D. E.; Lee, H. Nitronyl Nitroxide Radicals as Organic Memory Elements with Both n- and p-Type Properties. *Angew. Chem.*, *Int. Ed.* 2011, 50, 4414–4418.
- 14. Oyaizu, K.; Nishide, H. Radical Polymers for Organic Electronic Devices: A Radical Departure from Conjugated Polymers? *Adv. Mater.* **2009**, *21*, 2339–2344.
- 15. Clore, G. M. Practical Aspects of Paramagnetic Relaxation Enhancement in Biological Macromolecules. *Methods Enzymol.* **2015**, *564*, 485–497.
- 16. Nguyen, H. V.; Chen, Q.; Paletta, J. T.; Harvey, P.; Jiang, Y.; Zhang, H.; Boska, M. D.; Ottaviani, M. F.; Jasanoff, A.; Rajca, A.; Johnson, J. A. Nitroxide-Based Macromolecular Contrast Agents with Unprecedented Transverse Relaxivity and Stability for Magnetic Resonance Imaging of Tumors. ACS Cent. Sci. 2017, 3, 800–811.

- Rajca, A.; Wang, Y.; Boska, M.; Paletta, J. T.; Olankitwanit, A.; Swanson, M. A.; Mitchell, D. G.;
 Eaton, S. S.; Eaton, G. R.; Rajca, S. Organic Radical Contrast Agents for Magnetic Resonance
 Imaging. J. Am. Chem. Soc. 2012, 134, 15724–15727.
- 18. Pauling, L. The Nature of the Chemical Bond. Application of Results Obtained from the Quantum Mechanics and from a Theory of Paramagnetic Susceptibility to the Structure of Molecules. *J. Am. Chem. Soc.* **1931**, *53*, 1367–1400.
- 19. Pauli, W. Über den Zusammenhang des Abschlusses der Elektronengruppen im Atom mit der Komplexstruktur der Spektren. Zeitschrift für Physik 1925, 31, 765–783.
- 20. Ishida, T.; Iwamura, H. Bis[3-tert-butyl-5-(N-oxy-tert-butylamino)phenyl] nitroxide in a quartet ground state: a prototype for persistent high-spin poly[(oxyimino)-1,3-phenylenes]. *J. Am. Chem. Soc.* **1991**, *113*, 4238–4241.
- 21. Rajca, A.; Lu, K.; Rajca, S. High-spin polyarylmethyl polyradical: Fragment of a macrocyclic 2-strand based upon calix[4]arene rings. *J. Am. Chem. Soc.* **1997**, *119*, 10335–10345.
- 22. Rajca, A.; Rajca, S.; Wongsriratanakul, J. Very High-Spin Organic Polymer: π -Conjugated Hydrocarbon Network with Average Spin of $S \ge 40$. *J. Am. Chem. Soc.* **1999**, *121*, 6308–6309.
- 23. Adam, W.; Baumgarten, M.; Maas, W. A Hydrocarbon Hexaradical with Three Localized 1,3-Cyclopentanediyl Triplet Diradicals Linked by 1,3,5-Trimethylenebenzene as Ferromagnetic Coupler: Synthesis of the Azoalkane Precursor, Photochemical Generation of the Polyradical, and EPR Characterization of Its Septet-Spin Ground State. J. Am. Chem. Soc. 2000, 122, 6735–6738.
- 24. Shultz, D. A.; Fico, R. M., Jr; Lee, H.; Kampf, J. W.; Kirschbaum, K.; Pinkerton, A. A.; Boyle, P. D. Mechanisms of Exchange Modulation in Trimethylenemethane-type Biradicals: The Roles of Conformation and Spin Density. *J. Am. Chem. Soc.* 2003, 125, 15426–15432.
- 25. Rajca, A.; Wongsriratanakul, J.; Rajca, S. Organic Spin Clusters: Macrocyclic-Macrocyclic Polyarylmethyl Polyradicals with Very High-Spin S = 5 13. *J. Am. Chem. Soc.* **2004**, *126*, 6608–6626.

- 26. Rajca, A.; Wongsriratanakul, J.; Rajca, S.; Cerny, R. L. Organic Spin Clusters: Annelated Macrocyclic Polyarylmethyl Polyradicals and Polymer with Very High-Spin *S* = 6 18. *Chem. Eur. J.* **2004**, *10*, 3144–3157.
- 27. Krylov, A. I. Triradicals. J. Phys. Chem. A 2005, 109, 10638–10645.
- 28. Suzuki, S.; Furui, T.; Kuratsu, M.; Kozaki, M.; Shiomi, D.; Sato, K.; Takui, T.; Okada, K. Nitroxide-substituted nitronyl nitroxide and iminonitroxide. *J. Am. Chem. Soc.* **2010**, *132*, 15908–15910.
- 29. Neuhaus, P.; Sander, W. Isolation and Characterization of the Triradical 1,3,5-Trimethylenebenzene. *Angew. Chem. Int. Ed.* **2010**, *49*, 7277–7280.
- 30. Skórka, Ł.; Maurel, V.; Gosk, J. B.; Puźniak, R.; Mouesca, J. -M.; Irena Kulszewicz-Bajer, I. Highly Efficient Tuning of Ferromagnetic Spin Interactions in High-Spin Arylamine Structures by Incorporation of Spin Bearing Carbazole Units. *J. Phys. Chem. B* **2018**, *122*, 9584–9591.
- 31. Rajca, A.; Shiraishi, K.; Pink, M.; Rajca, S. Triplet (*S* = 1) Ground State Aminyl Diradical. *J. Am. Chem. Soc.* **2007**, *129*, 7232–7233.
- 32. Boratyński, P. J.; Pink, M.; Rajca, S.; Rajca, A. Isolation of the Triplet Ground State Aminyl Diradical. *Angew. Chem., Int. Ed.* **2010**, *49*, 5459–5462.
- 33. Rajca, A.; Olankitwanit, A.; Wang, Y.; Boratynski, P. J.; Pink, M.; Rajca, S. High-Spin S = 2 Ground State Aminyl Tetraradicals. *J. Am. Chem. Soc.* **2013**, *135*, 18205–18215.
- 34. Barone, V.; Boilleau, C.; Cacelli, I.; Ferretti, A.; Monti, S.; Prampolini, G. Structure-Properties Relationships in Triplet Ground State Organic Diradicals: A Computational Study. *J. Chem. Theory Comput.* **2013**, *9*, 300–307.
- 35. Barone, V.; Cacelli, I.; Ferretti, A.; Prampolini, G. Quantitative prediction and interpretation of spin energy gaps in polyradicals: the virtual magnetic balance. *Phys. Chem. Chem. Phys.* **2017**, *19*, 9039–9044.
- 36. Fang, S.; Lee, M.-S.; Hrovat, D. A.; Borden, W. A. Ab Initio Calculations Show Why *m*-Phenylene Is Not Always a Ferromagnetic Coupler. *J. Am. Chem. Soc.* **1995**, *117*, 6727–6731.

- 37. Rajca, A.; Shiraishi, K.; Rajca, S. Stable diarylnitroxide diradical with triplet ground state. *Chem. Commun.* **2009**, 4372–4374.
- 38. Rajca, A.; Shiraishi, K.; Boratynski, P. J.; Pink, M.; Miyasaka, M.; Rajca, S. Oxidation of Annelated Diarylamines: Analysis of Reaction Pathways to Nitroxide Diradical and Spirocyclic Products. *J. Org. Chem.* **2011**, *76*, 8447–8457.
- 39. Nguyen, H. M.; Dutta, A.; Morokuma, K.; Nguyen, M. T. Electronic structure of 1,3,5-triaminobenzene trication and related triradicals: doublet versus quartet ground state. *J. Chem. Phys.* **2005**, *122*, 154308.
- 40. Shimizu, D.; Osuka, A. A Benzene-1,3,5-Triaminyl Radical Fused with Zn-II-Porphyrins: Remarkable Stability and a High-Spin Quartet Ground State. *Angew. Chem., Int. Ed.* **2018**, *57*, 3733–3736.
- 41. Bushby, R. J.; Taylor, N.; Williams, R. A. Ferromagnetic spin-coupling 4, 4"-through *meta*-terphenyl: models for high-spin polymers. *J. Mater. Chem.* **2007**, *17*, 955–964.
- 42. Gallagher, N. M.; Bauer, J. J.; Pink, M.; Rajca, S.; Rajca, A. High-Spin Organic Diradical with Robust Stability. *J. Am. Chem. Soc.* **2016**, *138*, 9377–9380.
- 43. Gallagher, N.; Zhang, H.; Junghoefer, T.; Giangrisostomi, E.; Ovsyannikov, R.; Pink, M.; Rajca, S.; Casu, M. B.; Rajca, A. Thermally and Magnetically Robust Triplet Ground State Diradical. *J. Am. Chem. Soc.* **2019**, *141*, 4764–4774.
- 44. Shu, C.; Pink, M.; Junghoefer, T.; Nadler, E.; Rajca, S.; Casu, M. B.; Rajca, A. Synthesis and Thin Films of Thermally Robust Quartet (*S* = 3/2) Ground State Triradical. *J. Am. Chem. Soc.* **2021**, *143*, 5508–5518.
- 45. Zhang, S.; Pink, M.; Junghoefer, T.; Zhao, W.; Hsu, S.-N.; Rajca, S.; Calzolari, A.; Boudouris, B.
 W.; Casu, M. B.; Rajca, A. High-Spin (S = 1) Blatter-Based Diradical with Robust Stability and Electrical Conductivity. J. Am. Chem. Soc. 2022, 144, 6059–6070.
- 46. Tretyakov, E. V.; Zhivetyeva, S. I.; Petunin, P. V.; Gorbunov, D. E.; Gritsan, N. P.; Bagryanskaya, I. Y.; Bogomyakov, A. S.; Postnikov, P. S.; Kazantsev, M. S.; Trusova, M. E.; Shundrina, I. K.;

- Zaytseva, E. V.; Parkhomenko, D. A.; Bagryanskaya, E. G.; Ovcharenko, V. I. Ferromagnetically Coupled *S* = 1 Chains in Crystals of Verdazyl-Nitronyl Nitroxide Diradicals. *Angew. Chem., Int. Ed.* **2020**, *59*, 20704–20710.
- Tretyakov, E. V.; Petunin, P. V.; Zhivetyeva, S. I.; Gorbunov, D. E.; Gritsan, N. P.; Fedin, M. V.;
 Stass, D. V.; Samoilova, R. I.; Bagryanskaya, I. Y.; Shundrina, I. K.; Bogomyakov, A. S.; Kazantsev,
 M. S.; Postnikov, P. S.; Trusova, M. E.; Ovcharenko, V. I. Platform for High-Spin Molecules: A
 Verdazyl-Nitronyl Nitroxide Triradical with Quartet Ground State. J. Am. Chem. Soc. 2021, 143, 8164–8176.
- 48. Gu, Y.; Qiu, Z.; Müllen, K. Nanographenes and Graphene Nanoribbons as Multitalents of Present and Future Materials Science. *J. Am. Chem. Soc.* **2022**, *144*, 11499–11524.
- 49. Wang, T.; Berdonces-Layunta, A.; Friedrich, N.; Vilas-Varela, M.; Calupitan, J. P.; Pascual, J. I.; Peña, D.; Casanova, D.; Corso, M.; de Oteyza, D. G. Aza-Triangulene: On-Surface Synthesis and Electronic and Magnetic Properties. *J. Am. Chem. Soc.* **2022**, *144*, 4522–4529.
- 50. Su, J.; Fan, W.; Mutombo, P.; Peng, X.; Song, S.; Ondráček, M.; Golub, P.; Brabec, J.; Veis, L.; Telychko, M.; Jelínek, P.; Wu, J.; Lu, J. On-Surface Synthesis and Characterization of [7]Triangulene Quantum Ring. *Nano Lett.* **2021**, *21*, 861–867.
- 51. Mishra, S.; Beyer, D.; Eimre, K.; Liu, J.; Berger, R.; Gröning, O.; Pignedoli, C. A.; Müllen, K.; Fasel, R.; Feng, X.; Ruffieux, P. Synthesis and Characterization of Π-Extended Triangulene. *J. Am. Chem. Soc.* 2019, 141, 10621–10625.
- 52. Jie Su, Wei Fan, Pingo Mutombo, Xinnan Peng, Shaotang Song, Martin Ondráček, Pavlo Golub, Jiří Brabec, Libor Veis, Mykola Telychko, Pavel Jelínek*, Jishan Wu*, and Jiong Lu*
- 53. Ruffieux, P.; Wang, S.; Yang, B.; Sanchez-Sanchez, C.; Liu, J.; Dienel, T.; Talirz, L.; Shinde, P.; Pignedoli, C. A.; Passerone, D.; Dumslaff, T.; Feng, X.; Mullen, K.; Fasel, R. On-surface synthesis of graphene nanoribbons with zigzag edge topology. *Nature* **2016**, *531*, 489–492.

- 54. Slota, M.; Keerthi, A.; Myers, W. K.; Tretyakov, E.; Baumgarten, M.; Ardavan, A.; Sadeghi, H.; Lambert, C. J.; Narita, A.; Mullen, K.; Bogani, L. Magnetic edge states and coherent manipulation of graphene nanoribbons. *Nature* **2018**, *557*, 691–695.
- 55. Mishra, S.; Catarina, G.; Wu, F.; Ortiz, R.; Jacob, D.; Eimre, K.; Ma, J.; Pignedoli, C. A.; Feng, X.; Ruffieux, P.; Fernández-Rossier, J.; Fasel, R. Observation of fractional edge excitations in nanographene spin chains. *Nature* **2021**, *598*, 287–292.
- 56. Hieulle, J.; Castro, S.; Friedrich, N.; Vegliante, A.; Lara, F. R.; Sanz, S.; Rey, D.; Corso, M.; Frederiksen, T.; Pascual, J. I.; Peña, D. On-Surface Synthesis and Collective Spin Excitations of a Triangulene-Based Nanostar. *Angew. Chem., Int. Ed.* 2021, 60, 25224–25229.
- 57. Mishra, S.; Fatayer, S.; Fernández, S.; Kaiser, K.; Peña, D.; Gross, L. Nonbenzenoid High-Spin Polycyclic Hydrocarbons Generated by Atom Manipulation. *ACS Nano* **2022**, *16*, 3264–3271.
- 58. Arikawa, S.; Shimizu, A.; Shiomi, D.; Sato, K.; Shintani, R. Synthesis and Isolation of a Kinetically Stabilized Crystalline Triangulene. *J. Am. Chem. Soc.* **2021**, *143*, 19599–19605.
- 59. Wei, H.; Hou, X.; Xu, T.; Zou, Y.; Li, G.; Wu, S.; Wu, J. Solution-Phase Synthesis and Isolation of An Aza-Triangulene and Its Cation in Crystalline Form. *Angew. Chem. Int. Ed.* **2022**, e202210386 (1-6) Published on Aug. 22, 2022; DOI: https://doi.org/10.1002/anie.202210386
- 60. Błoński, P.; Tuček, J.; Sofer, Z.; Mazánek, V.; Petr, M.; Pumera, M.; Otyepka, M.; Zbořil, R. Doping with Graphitic Nitrogen Triggers Ferromagnetism in Graphene. *J. Am. Chem. Soc.* **2017**, *139*, 3171–3180.
- 61. Rajca, A; Rajca, S. Intramolecular antiferromagnetic vs ferromagnetic spin coupling through the biphenyl unit. *J. Am. Chem. Soc.* **1996**, *118*, 8121–8126.
- 62. Rajca, A.; Wongsriratanakul, J.; Rajca, S. High-Spin Organic Polyradicals as Spin Clusters: Ferromagnetic Spin Coupling through Biphenyl Unit in Polyarylmethyl Tri-, Penta-, Hepta-, and Hexadecaradicals. *J. Am. Chem. Soc.* **1997**, *119*, 11674–11686.
- 63. Rajca, S.; Rajca, A.; Wongsriratanakul, J.; Butler, P.; Choi, S. Organic Spin Clusters. A Dendritic-Macrocyclic Poly(arylmethyl) Polyradical with Very High Spin of S=10 and Its Derivatives:

- Synthesis, Magnetic Studies, and Small-Angle Neutron Scattering. *J. Am. Chem. Soc.* **2004**, *126*, 6972–6986.
- 64. Schreiner, P. R. Quantum Mechanical Tunneling Is Essential to Understanding Chemical Reactivity. *Trends in Chemistry*, **2020**, *2*, 980–989.
- 65. Wang, Y.; Olankitwanit, A.; Rajca, S.; Rajca, A. Intramolecular Hydrogen Atom Transfer in Aminyl Radical at Room Temperature with Large Kinetic Isotope Effect. *J. Am. Chem. Soc.* **2017**, *139*, 7144–7147.
- Roberts, J. R.; Ingold, K. U. Kinetic applications or electron paramagnetic resonance spectroscopy.
 X. Reactions of some alkylamino radicals in solution. *J. Am. Chem. Soc.* 1973, 95, 3228–3235.
- 67. Bock, H.; Rajaoarivelo, M.; Clavaguera, S.; Grelet, E. An Efficient Route to Stable Room-Temperature Liquid-Crystalline Triphenylenes. *Eur. J. Org. Chem.* **2006**, 2889–2893.
- 68. Levi, Z. U.; Tilley, T. D. Synthesis and Electronic Properties of Extended, Fused-Ring Aromatic Systems Containing Multiple Pentalene Units. *J. Am. Chem. Soc.* **2010**, *132*, 11012–11014.
- 69. Rajca, A.; Boratynski, P. J.; Olankitwanit, A.; Shiraishi, K.; Pink, M.; Rajca, S. Ladder Oligo(*m*-aniline)s: Derivatives of Azaacenes with Cross-Conjugated π-Systems. *J. Org. Chem.* **2012**, 77, 2107–2120.
- 70. Shiraishi, K.; Rajca, A.; Pink, M.; Rajca, S. π-Conjugated Conjoined Double Helicene via a Sequence of Three Oxidative CC- and NN-Homocouplings. *J. Am. Chem. Soc.* **2005**, *127*, 9312–9313.
- 71. Connelly, N. G.; Geiger, W. E. Chemical Redox Agents for Organometallic Chemistry. *Chem. Rev.* **1996**, *96*, 877–910.
- 72. Olankitwanit, A.; Pink, M.; Rajca, S.; Rajca, A. Synthesis of Aza-m-Xylylene Diradicals with Large Singlet-Triplet Energy Gap and Statistical Analyses of their EPR Spectra. *J. Am. Chem. Soc.* **2014**, *136*, 14277–14288.
- 73. Li, Z.; Zhi, L.; Lucas, N. T.; Wang, Z. Triangle-shaped polycyclic aromatics based on tribenzocoronene: facile synthesis and physical properties. *Tetrahedron* **2009**, *65*, 3417–3424.

- 74. Mercury 2.3, http://www.ccdc.cam.ac.uk/mercury/: Macrae, C. F.; Bruno, I. J.; Chisholm, J. A.; Edgington, P. R.; McCabe, P.; Pidcock, E.; Rodriguez-Monge, L.; Taylor, R.; van de Streek J.; Wood, P. A. New Features for the Visualization and Investigation of Crystal Structures. *J. Appl. Cryst.* 2008, 41, 466–470.
- Frisch, M. J.; Trucks, G. W.; Schlegel, H. B.; Scuseria, G. E.; Robb, M. A.; Cheeseman, J. R.; Scalmani, G.; Barone, V.; Mennucci, B.; Petersson, G. A.; Nakatsuji, H.; Caricato, M.; Li, X.; Hratchian, H. P.; Izmaylov, A. F.; Bloino, J.; Zheng, G.; Sonnenberg, J. L.; Hada, M.; Ehara, M.; Toyota, K.; Fukuda, R.; Hasegawa, J.; Ishida, M.; Nakajima, T.; Honda, Y.; Kitao, O.; Nakai, H.; Vreven, T.; Montgomery, Jr., J. A.; Peralta, J. E.; Ogliaro, F.; Bearpark, M.; Heyd, J. J.; Brothers, E.; Kudin, K. N.; Staroverov, V. N.; Kobayashi, R.; Normand, J.; Raghavachari, K.; Rendell, A.; Burant, J. C.; Iyengar, S. S.; Tomasi, J.; Cossi, M.; Rega, N.; Millam, N. J.; Klene, M.; Knox, J. E.; Cross, J. B.; Bakken, V.; Adamo, C.; Jaramillo, J.; Gomperts, R.; Stratmann, R. E.; Yazyev, O.; Austin, A. J.; Cammi, R.; Pomelli, C.; Ochterski, J. W.; Martin, R. L.; Morokuma, K.; Zakrzewski, V. G.; Voth, G. A.; Salvador, P.; Dannenberg, J. J.; Dapprich, S.; Daniels, A. D.; Farkas, Ö.; Foresman, J. B.; Ortiz, J. V.; Cioslowski, J.; Fox, D. J. *Gaussian 09*. Gaussian, Inc.: Wallingford CT, 2009.
- 76. Frisch, M. J.; Trucks, G. W.; Schlegel, H. B.; Scuseria, G. E.; Robb, M. A.; Cheeseman, J. R.; Scalmani, G.; Barone, V.; Petersson, G. A.; Nakatsuji, H.; Li, X.; Caricato, M.; Marenich, A. V.; Bloino, J.; Janesko, B. G.; Gomperts, R.; Mennucci, B.; Hratchian, H. P.; Ortiz, J. V.; Izmaylov, A. F.; Sonnenberg, J. L.; Williams-Young, D.; Ding, F.; Lipparini, F.; Egidi, F.; Goings, J.; Peng, B.; Petrone, A.; Henderson, T.; Ranasinghe, D.; Zakrzewski, V. G.; Gao, J.; Rega, N.; Zheng, G.; Liang, W.; Hada, M.; Ehara, M.; Toyota, K.; Fukuda, R.; Hasegawa, J.; Ishida, M.; Nakajima, T.; Honda, Y.; Kitao, O.; Nakai, H.; Vreven, T.; Throssell, K.; Montgomery, J. A., Jr.; Peralta, J. E.; Ogliaro, F.; Bearpark, M. J.; Heyd, J. J.; Brothers, E. N.; Kudin, K. N.; Staroverov, V. N.; Keith, T. A.; Kobayashi, R.; Normand, J.; Raghavachari, R.; Rendell, A. P.; Burant, J. C.; Iyengar, S. S.; Tomasi, J.; Cossi, M.; Millam, J. M.; Klene, M.; Adamo, C.; Cammi, R.; Ochterski, J. W.; Martin, R. L.; Morokuma, K.;

- Farkas, O.; Foresman, J. B.; Fox, D. J. *Gaussian 16*, Revision A.03; Gaussian, Inc.: Wallingford, CT, 2016.
- 77. Lodewyk, M. W.; Siebert, M. R.; Tantillo, D. J. Computational Prediction of ¹H and ¹³C Chemical Shifts: A Useful Tool for Natural Product, Mechanistic, and Synthetic Organic Chemistry. *Chem. Rev.* **2012**, *112*, 1839–1862.
- 78. Lacerda, Jr., E. G.; Kamounah, F. S.; Coutinho, K.; Sauer, S. P. A.; Hansen, P. E.; Hammerich, O. Computational Prediction of ¹H and ¹³C NMR Chemical Shifts for Protonated Alkylpyrroles: Electron Correlation and Not Solvation is the Salvation. *ChemPhysChem* **2019**, *20*, 78–91.
- 79. Nguyen, T. T. ¹H/¹³C chemical shift calculations for biaryls: DFT approaches to geometry optimization. *R. Soc. Open Sci.* **2021**, *8*, 210954. https://doi.org/10.1098/rsos.210954
- 80. Rajca, A.; Olankitwanit, A.; Rajca, S. Triplet Ground State Derivative of Aza-m-Xylylene Diradical with Large Singlet–Triplet Energy Gap. *J. Am. Chem. Soc.* **2011**, *133*, 4750–4753.
- 81. Stoll, S.; Schweiger, A. EasySpin, a comprehensive software package for spectral simulation and analysis in EPR. *J. Magn. Reson.* **2006**, *178*, 42–55.
- 82. Shu, C.; Zhang, H.; Olankitwanit, A.; Rajca, S.; Rajca, A. High-Spin Diradical Dication of Chiral π-Conjugated Double Helical Molecule. *J. Am. Chem. Soc.* **2019**, *141*, 17287–17294.
- 83. Neese, F. The ORCA program system. Wiley Interdiscip. Rev.: Comput. Mol. Sci. 2012, 2, 73–78.
- 84. Sinnecker, S.; Neese, F. Spin-Spin Contributions to the Zero-Field Splitting Tensor in Organic Triplets, Carbenes and Biradicals A Density Functional and Ab Initio Study. *J. Phys. Chem. A* **2006**, *110*, 12267–12275.
- 85. Morton, J. R. Electron Spin Resonance Spectra of Oriented Radicals. Chem. Rev. 1964, 64, 453–471.
- 86. Belorizky, E.; Fries, P. H. Exact solutions for simple spin clusters with isotropic Heisenberg exchange interactions. *J. Chim. Phys. (Paris)* **1993**, *90*, 1077–1100.
- 87. Rajca, A.; Mukherjee, S.; Pink, M.; Rajca, S. Exchange Coupling Mediated Through-Bonds and Through-Space in Conformationally Constrained Polyradical Scaffolds: Calix[4]arene Nitroxide Tetraradicals and Diradical. *J. Am. Chem. Soc.* **2006**, *128*, 13497–13507.

- 88. Westman, A. E. R.; DeLury, D. B. The Differential Equations of Consecutive Reactions. *Can. J. Chem.* **1956**, *34*, 1134–1138.
- 89. Blanksby, S. J.; Ellison, G. B. Bond Dissociation Energies of Organic Molecules. *Acc. Chem. Res.* **2003**, *36*, 255–263.
- 90. Yamaguchi, K.; Jensen, F.; Dorigo, A.; Houk, K. N. A Spin Correction Procedure for Unrestricted Hartree–Fock and Møller–Plesset Wavefunctions for Singlet Diradicals and Polyradicals. *Chem. Phys. Lett.* **1988**, *149*, 537–542.
- 91. Trinquier, G.; Suaud, N.; Malrieu, J.-P. Theoretical Design of High-Spin Polycyclic Hydrocarbons. *Chem. Eur. J.* **2010**, *16*, 8762–8772.
- 92. Quast, H.; Nüdling, W.; Klemm, G.; Kirschfeld, A.; Neuhaus, P.; Sander, W.; Hrovat, D. A.; Borden, W. T. A Perimidine-Derived Non-Kekulé Triplet Diradical. *J. Org. Chem.* **2008**, *73*, 4956–4961.
- 93. Fukuzaki, E.; Nishide, H. 2,6,10-Tris(dianisylaminium)-3,7,11-tris(hexyloxy)triphenylene: A Robust Quartet Molecule at Room Temperature. *Org. Lett.* **2006**, *8*, 1835–1838.
- 94. Evans, D. F. The determination of the paramagnetic susceptibility of substances in solution by nuclear magnetic resonance. *J. Chem. Soc.* **1959**, 2003–2005.
- 95. Live, D. H.; Chan, S. I. Bulk susceptibility corrections in nuclear magnetic resonance experiments using superconducting solenoids. *Anal. Chem.***1970**, *42*, 791–792.

TOC Graphics

